The Thesis Committee for Sang Hyon Han
Certifies that this is the approved version of the following thesis:

Investigating the Geochemical Alterations in an Aquifer Due to Long-Term Sequestration of CO_2 using Time-Lapse Seismic Information

APPROVED BY
SUPERVISING COMMITTEE:

Co-Supervisor:

Kamy Sepehrnoori

Co-Supervisor:

Sanjay Srinivasan

Mrinal Sen

Investigating the Geochemical Alterations in an Aquifer Due to Long-Term Sequestration of CO_2 using Time-Lapse Seismic Information

by

Sang Hyon Han, B.S.

Thesis

Presented to the Faculty of the Graduate School of

The University of Texas at Austin

in Partial Fulfillment

of the Requirements

for the Degree of

Master of Science in Engineering

The University of Texas at Austin

December 2015

Dedication

To my family

Acknowledgements

First and foremost, I would like to thank my advisor, Dr. Sanjay Srinivasan, for his guidance and support and for providing me the opportunity to work on this interesting research topic. Without his patience, inspirations, and vision for this work, I would have been easily lost. He is also very kind and caring, and I am so thankful for having him as my advisor.

I also would like to thank Dr. Sen, Dr. Spikes, and Russell Carter from the Jackson School for providing me the inverted seismic data and for patiently teaching me about the geophysics concepts. Great appreciation also to Dr. Sen and Dr. Sepehrnoori for devoting their time to review my thesis and for providing valuable feedbacks.

Lastly, I would like to thank all the people I met in Austin for the good memories.

Abstract

Investigating the Geochemical Alterations in an Aquifer Due to Long-Term Sequestration of CO_2 using Time-Lapse Seismic Information

Sang Hyon Han, M.S.E.

The University of Texas at Austin, 2015

Co-Supervisor: Kami Sepehrnoori

Co-Supervisor: Sanjay Srinivasan

The effects of chemical interaction between injected CO_2, brine, and formation rocks are often ignored in sequestration studies because chemical reactions are assumed to be localized to carbonate rocks that make up only a small proportion of the potential reservoirs. It is conjectured in this work that long-term exposure of certain types of clays and cement material to CO_2-brine mixtures can induce chemical reactions and subsequent alteration of rock properties that can be subsequently detected in time-lapse seismic surveys. This is demonstrated using a case-study structured after the Cranfield field injection site. Geochemical alterations of the reservoir rock are quantified by performing reactive transport simulations and subsequently using rock physics models to translate the altered petrophysical properties into seismic responses. The study quantifies the long-term geochemical effects of CO_2 injection on the seismic response and conversely, presents an approach to invert the reservoir regions contacted by the CO_2-saturated brine based on the observed seismic response.

Time lapse or passive seismic monitoring is an effective method for mapping the progress of the CO_2 plume through the subsurface. But, because of the lack of resolution of the seismic information, it is necessary to use the seismic information together with prior geologic knowledge about the surface in order to identify if there is any migration of CO_2 into regions that might be deemed sensitive e.g. overlying aquifers or faults. Because of uncertainties in the prior geologic description of the reservoir, the feasibility of implementing a model selection process is explored in this work. The model selection procedure utilizes the observed well data and reference seismic map to select a subset of models. The flow simulation of CO_2 injection and forward seismic modeling were repeated for the newly generated reservoir models, and the seismic responses were compared for the reaction and non-reaction cases.

The study showed that the effects of geochemical reactions on petrophysical properties and resultant spatial distribution of fluid saturation were visible in the seismic response. Major differences in seismic responses were detected in regions of the reservoir where significant amount of minerals were dissolved and precipitated. These regions were at the top of the reservoir due to the reactions caused by the buoyant CO_2 plume. The presence of carbonate facies, even in small proportion, plays an important role in geochemical reactions and their effect is manifested at the seismic scale. The unique model selection methodology presented in this thesis is efficient at detecting the important features in the seismic and injection response that is induced by the geochemical alterations occurring in the reservoir. The results of this time-lapse study can provide new interpretation of events observed in time-lapse seismic data that might lead to a better assessment of leakage pathways and other risks.

Table of Contents

List of Tables

List of Figures

Chapter 1: Introduction

1.1 Overview

According to the United States Environmental Protection Agency (2014), the surface temperature of Earth has increased by 1.4^{o}F over the last century due to global warming . Over the past 800,000 years, there have been cycles of increase and decrease in surface temperature, which correlates well to carbon dioxide (CO_2) concentration in the atmosphere. However, in recent times, a steeper increase in temperature and CO_2 concentration has been observed as compared to the fluctuations observed in the previous cycles. Using various geologic and engineering models and calculations, scientists have discovered that the recent increase in greenhouse gases (i.e. CO_2) in the atmosphere is due to a significant amount of fossil fuels being burned since the Industrial Revolution (Wolff et al., 2014). The use of fossil fuels is expected to continue to increase until about year 2030. Consequently, the energy industry and government agencies are investigating many technologies for reducing CO_2 level in the atmosphere. One of the proposed methods is carbon sequestration, in which CO_2 is injected and stored in the deep subsurface.

CO_2 storage in a deep formation requires structural and geochemical trapping mechanisms in order to ensure that the CO_2 remains sequestered in the subsurface for a long duration. Structural trapping mechanism involves physical trapping of the CO_2 plume due to buoyancy forces and the capillary barrier exerted by the reservoir seal (Lu et al., 2013; Mandalaparty et al., 2011). When CO_2 is injected, its low density relative to in situ formation fluids, typically brine, causes it to migrate upward due to buoyancy. Capillary force is due to interfacial effects between the CO_2 and the rock mineral that prevents the CO_2 from entering the pore space of the formation seal until an entry pressure is attained. Geochemical trapping involves chemical interactions between rocks, formation fluids, and

injected CO_2 (Lu et al., 2012). When CO_2 is injected, it dissolves in brine and raises the acidity (or lowers the pH) of formation fluids, initiating geochemical alteration of reservoir rocks by mineral dissolution and precipitation. CO_2 is thereby stored in the formation in the form of a new material formed as a result of precipitation. .

Currently, there are various analytical models and numerical simulators like CMG-GEM and PHREEQC (Computer Modelling Group Ltd., 2013; Parkhurst and Appelo, 2013; Singh and Srinivasan, 2014) that can account for the geologic heterogeneity in reservoirs and compute the physical behavior of the CO_2 plume. There are numerous papers examining the physics and chemistry of carbon sequestration. However, these works do not take the results pertaining to the alterations in properties of the reservoir all the way to its impact on seismic wave propagation and the consequent interpretation and modeling implications. The research presented in this thesis aims to address this shortcoming.

1.2 Research Objectives

Siliciclastic reservoirs are great potential sites for CO_2 sequestration because they are composed mainly of non-reactive quartz sandstones. Consequently, chemical reaction between injected CO_2, brine, and formation rocks are often ignored in sequestration studies. Many reservoirs, however, do contain a small amount of carbonate rocks, which are reactive and can cause geochemical alterations of the reservoir rocks. In addition the cement material between rock-grains may in some cases be reactive and this can also result in alterations to the mechanical properties of the rock. The thesis explores this issue by simulating and quantifying the effect of long-term geochemical effects of CO_2 injection on seismic response. Subsequently an approach to model the reservoir regions contacted by the CO_2-saturated brine by inverting the seismic response is presented. The application of this approach is demonstrated using the data for the Cranfield field injection site.

The study showed that the effects of geochemical reactions on petrophysical properties and resultant spatial distribution of fluid saturation are detectable in the seismic response. Through this time-lapse study, we are able to provide new interpretation of events observed in time-lapse seismic data that might lead to a better assessment of leakage pathways and other risks.

1.3 THESIS OUTLINE

Chapter 2 presents a brief review of the relevant literature pertaining to geochemical reactions associated with injection of CO_2 in the subsurface. The main reactions of CO_2 with reservoir rocks and past experimental and modeling works are reviewed. Some basic concepts in rock physics modeling and recommended techniques presented in literature are also introduced. In addition, the past works on time-lapse seismic modeling and workflows are discussed. Lastly, the research specifically performed using data from the Cranfield site are reviewed.

Chapter 3 describes the models and methods used in this thesis. It discusses the geostatistical methods, geochemical models, and rock physics models that have been used to characterize a CO_2 sequestration site and the flow and transport model used to simulate reactions and CO_2 plume migration. The forward seismic model used to generate synthetic seismograms and the concept of discrete Fréchet distance used to compare seismic signatures from different models are also discussed.

Chapter 4 presents the development of a reference model using the data and methods discussed in Chapter 3. Through model selection the subset of prior reservoir models that closely match the reference model can be identified and subsequently, using model expansion, additional models can be generated that share the variogram

characteristics of the selected set of models. This model selection and expansion method is also discussed in this chapter.

In Chapter 5, the model selection and uncertainty quantification process is applied using actual time-lapse seismic information for Cranfield. The inverted seismic impedance information at initial time is first used to generate a suite of prior models and then apply the model selection and expansion process discussed in Chapter 4. Reservoir models with different carbonates rock proportion were specified as part of the prior model and were subsequently refined. The best models were used to assess the long-term geochemical effects in the aquifer.

Chapter 6 concludes the thesis and introduces ideas for future research.

Chapter 2: Literature Review

One of the viable methods to reduce the concentration of greenhouse gases in the atmosphere is carbon sequestration. In this process, carbon dioxide (CO_2) is captured and stored in deep subsurface aquifers resulting in mechanical and geochemical alterations of subsurface formations. Mechanical changes include pressure change due to injection of large volumes of CO_2 into a reservoir already filled with fluids and the accompanying change in density of the formation. There is considerable research performed around the world investigating the physics of CO_2 migration and how it effects the properties of reservoirs. Geochemical alteration of reservoirs involves reactions between in situ and injected fluid and formation rocks. During reactions, reservoir rocks (e.g. carbonates and sandstones) are either dissolved or precipitated resulting in alteration to rock frames. This chapter reviews previous experimental and simulation works performed to understand the geochemical reactions associated with CO_2 injection into carbonates and sandstones. It also introduces how these works have been applied to carbon sequestration at Cranfield.

2.1 Geochemistry of CO_2 Sequestration

When CO_2 is injected into a saline aquifer, it dissolves in formation brine and lowers the pH, triggering mineral reactions. Mineral reactions, that lead to dissolution and/or precipitation of reservoir rocks, permanently reshape pore network of the formation, and that is very difficult to model (Vanorio et al., 2011). Imaging techniques such as scanning-electron microscopy (SEM) and CT scanning, are widely used to observe the alterations at pore scale. It is observed using SEM images and CT scans that CO_2-saturated brine in a carbonate rock initiates dissolution mainly in the grain-coating cement, and this is followed by the formation of micropores and wormholes that result in a decrease in the acoustic velocity of the rock (Gharbi et al. 2013; Grombacher, et al., 2011; Vialle and

Vanorio 2011; Egermann et al., 2005). Figure 2-1, adopted from an experimental work by Vanorio et al. (2011) shows SEM and CT scan images of a carbonate core sample dissolved by CO_2-saturated brine. Porosity enhancement due to formation of micropores is clearly observed. At reservoir scale, these changes are accompanies by increase in porosity.

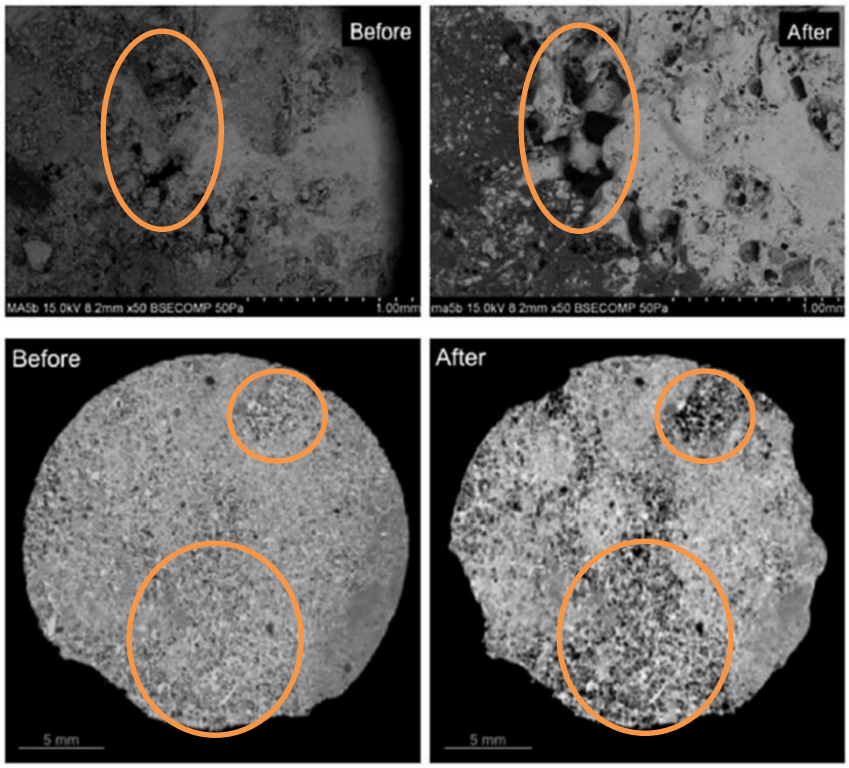

Figure 2-1: CT scan images of a carbonate core sample dissolved by CO2-saturated brine. Porosity enhancement due to formation of micropores is clearly observed (Vanorio et al., 2011) within the marked regions.

2.1.1 Geochemical Reactions

CO_2 has a very high solubility in brine. When CO_2 is injected as a gas phase into a saline aquifer, it dissolves in brine to become an aqueous solution as shown in Equation 2.1. It then forms carbonic acid as it becomes equilibrated with brine (Equation 2.2).

Carbonic acid further dissociates into hydrogen and bi-carbonate ions as shown in Equation 2.3 (De Silva et al. 2015).

$$CO_2(g) \rightarrow CO_2(aq) \quad \text{.....(2.1)}$$

$$CO_2(g) + H_2O(l) \leftrightarrow H_2CO_3(aq) \quad \text{.....(2.2)}$$

$$H_2CO_3(aq) \leftrightarrow H^+(aq) + HCO_3^-(aq) \quad \text{.....(2.3)}$$

The formation of hydrogen ions lowers pH of aquifer brine and triggers mineral reactions as studied in many experimental and simulation works. Gunter et al. (1996) investigated CO_2 injection into the Glauconitic Sandstone aquifer in the Alberta Sedimentary Basin. They discovered that small amount of anorthite in the rock accelerated reactions and produced Ca^{2+} (Equation 2.4), which then reacted with bicarbonate ions formed in Equation 2.3 to precipitate calcite and kaolinite (Equation 2.5).

$$\underbrace{CaAl_2Si_2O_8(s)}_{anorthite} + 2H^+(aq) + H_2O(l) \rightarrow Ca^{2+}(aq) + \underbrace{Al_2Si_2O_5(OH)_4(s)}_{kaolinite} \quad \text{.....(2.4)}$$

$$\underbrace{CaAl_2Si_2O_8(s)}_{anorthite} + CO_2(g) + 2H_2O(l) \rightarrow \underbrace{CaCO_3(s)}_{calcite} + \underbrace{Al_2Si_2O_5(OH)_4(s)}_{kaolinite} \quad \text{.....(2.5)}$$

In the first carbon sequestration project in China, Wang et al. (2013) observed three different reactions taking place simultaneously when feldspar was dissolved in solution (Equations 2.6, 2.7 and 2.8) in the Erdos site. K-feldspar, albite, and anorthite each reacted according to their rate law.

$$K - feldspar + 4H_2O + 4H^+ \rightarrow K^+ + Al^{3+} + 3H_4SiO_4 \quad \text{.....(2.6)}$$

$$Albite + 4H_2O + 4H^+ \rightarrow Na^+ + Al^{3+} + 3H_4SiO_4 \quad \text{.....(2.7)}$$

$$Anorhite + 8H^+ \rightarrow Ca^{2+} + Al^{3+} + 2H_4SiO_4 \quad \text{.....(2.8)}$$

Mito et al. (2008) performed field study on CO_2 injection at a sandstone reservoir at Nagaoka, Japan. Although quartz was the most dominant mineral in the reservoir, its

slow reaction rate yielded the dissolutions of chlorite and plagioclase and those were the sources of Ca, Mg, Fe, and Si (Equations 2.9 and 2.10).

$$Plagioclase + 2H^+ + 3H_2O \rightarrow Ca^{2+} + 2Al\left(OH\right)_3 + 2H_4SiO_4 + NaAlSi_3O_4 \text{ .....(2.9)}$$

$$Chlorite + 20H^+ \rightarrow 5Mg^{2+} + 5Fe^{2+} + 4Al\left(OH\right)_3 + 6H_4SiO_4 \text{ ……...……...(2.10)}$$

Ngheim et al. (2004) used a commercial compositional simulator, CMG-GEM, to model carbon sequestration in a reservoir that consists mostly of quartz (71%) and of fractions of kaolinite, calcite, anorthite, dolomite, illite, and feldspar. Ngheim et al. injected about 0.2 pore volume of CO_2 into the reservoir in two-year period and observed the migration of CO_2 and mineral reactions for another 398 years. Similar to the sandstone reservoir in Nagaoka, relatively fast reaction rates in carbonates (i.e. calcite and dolomite) dominated other reactions, in terms of their effects on petrophysical properties such as porosity. In addition to the carbonation reactions in Equations 2.1, 2.2, and 2.3, calcite and dolomite reactions occurred as shown in the following two equations (2.11 and 2.12):

$$Calcite + H^+ \leftrightarrow Ca^{2+} + HCO_3^- \text{ ……...……..…(2.11)}$$

$$Dolomite + 2H^+ \leftrightarrow Ca^{2+} + Mg^{2+} + 2HCO_3^- \text{ ……...…….(2.12)}$$

Most of the CO_2 was observed to be dissolved in 150 years. The reactions, however, continued to take place beyond that time. Calcite and dolomite dissolved for the first 98 years before they started to precipitate. After 355 years, the net precipitation of calcite was positive.

2.2 ROCK PHYSICS MODELING OF CO_2 SEQUESTRATION RELATED EFFECTS

From the previous experimental and simulation studies discussed it is evident that CO_2-brine-rock interactions result in changes in concentrations of aqueous solutions and consequent petrophysical alterations. However, in most of these studies, the changes were

observed in laboratory scales. It is necessary to be able to discern these effects at the field scale. Rock physics models can be used to quantify the relationship between petrophysical properties and acoustic properties of reservoirs, in preparation for inferring the effects of geochemical alterations at field scale using seismic information.

2.2.1 Gassmann Fluid Substitution Model

Gassmann (1951) developed a fluid substitution model that predicts seismic velocities in saturated rocks when one fluid replaces the original fluid in place (e.g. CO_2 replacing in situ fluids during injection processes or water replacing hydrocarbons in a reservoir during water flooding). He derived equations (2.13 and 2.14) that quantify induced pore-pressure changes due to compression, in terms of bulk modulus of the saturated rocks.

$$\frac{K_{dry}}{K_0 - K_{sat}} = \frac{K_{dry}}{K_0 - K_{dry}} + \frac{K_{fl}}{\phi(K_0 - K_{fl})}, \quad \text{.....(2.13)}$$

$$\frac{1}{\mu_{dry}} = \frac{1}{\mu_{sat}}, \quad \text{.....(2.14)}$$

where K_{dry}, K_{sat}, K_0, and K_{fl} are bulk moduli of dry rock, saturated rock, mineral, and fluid, respectively; ϕ is porosity; and μ_{dry} and μ_{sat} are shear moduli of dry and saturated rocks.

However, the model assumes that the rocks are isotropic with homogeneous elastic moduli. The model also assumes low-frequency (<100Hz) acoustic environment so that there is sufficient time to equilibrate induced pore pressure, which makes the model appropriate at seismic scale (Mavko et al., 2009). The implication of the first assumption is that there should be no chemical interaction between rocks and fluids because reactions can render the rocks anisotropic by altering pore structures. These assumptions further imply that shear moduli of rocks do not mechanically rely on the presence of fluid and therefore remains constant when a new fluid is introduced (Berryman, 1999).

2.2.2 Effective Medium Theories

To quantify the relationship between petrophysical properties such as porosity and elastic properties such as bulk moduli, the effective medium theories that constrain the value for K_{sat} of saturated media can be used. The simplest bounds are the Voigt upper bound (Voigt, 1906) and the Reuss lower bound (Reuss, 1929) shown in Equations 2.15 and 2.16, respectively.

$$K_{Voigt} = \sum_{i=1}^{N} f_i K_i, \quad \text{.....(2.15)}$$

$$K_{Reuss} = \sum_{i=1}^{N} \frac{f_i}{K_i}, \quad \text{.....(2.16)}$$

where f_i is the fraction of material i and K_i is the bulk modulus of material i. The bulk modulus of any combination of two materials including the ones in different phases has to be within these bounds.

There are numerous models and theories that are used to determine where within the Voigt and Reuss bounds, the rocks of interest lie. The types of pore shapes, cements, and mineralogy, etc. should be carefully examined to choose the right model for the target reservoir. The Kuster-Toksöz model (Kuster and Toksöz, 1974; Berryman, 1995) uses an elastic wave scattering theory to express effective moduli corresponding to various pore shapes (e.g. spheres, needles, disks, and penny cracks). The differential effective medium (DEM) theory (Roscoe, 1952; Boucher, 1974) considers a formation rock as a host rock and treats pore or fluid as a second-phase material that is incrementally added onto the first-phase host rock. Like the Kuster-Toksöz, it expresses effective moduli corresponding to different pore shapes. The cementation theory (Dvorkin and Nur, 1996) can be used to derive effective moduli of poorly-cemented dry rock. Hertz-Mindlin contact theory

(Mindlin 1949; Dvorkin and Nur, 1996) is used for uncemented rocks near critical porosity, the porosity at which grains become suspended.

The above models are appropriate at ultrasonic laboratory environments because they account for the details of pore geometry at very high frequencies, meaning that there is not enough time for wave-induced pore-pressure to equilibrate (Mavko et al., 2009). At the seismic scale, Mavko et al. (2009) recommend finding the effective moduli of dry rock and then using fluid substitution to compute the effective moduli of saturated rocks.

2.3 TIME-LAPSE SEISMIC MODELING AND WORKFLOW

Matching the processed time-lapse seismic responses to the real seismic data can provide important geologic information about the formation. Lygren et al. (2002) investigated the possible reasons for CO_2 flowing through the shale layers in the Sleipner CO_2 sequestration site. They created two possible scenarios for the structure of the shale layers: one with holes vertically running across the layer and the other with semi-permeable characteristics. Flow simulations were run using models for both scenarios, and the observed mechanical behaviors were translated into the acoustic impedance using rock physics models, at two different time steps that the seismic data was available. By comparing the results with the real time-lapse seismic data, they found the shale model that yielded the seismic response similar to the real data, concluding that the shale layers in the Sleipner site may be semi-permeable.

Cui and Hoffman (2013) performed a dynamic reservoir characterization of Delhi Field, a CO_2 EOR site, by utilizing time-lapse seismic data in history matching. An initial model was created by applying sequential Gaussian simulation using well logs and core measurements. Flow simulation was run on the initial model, and the corresponding time-lapse acoustic impedances were computed. With an objective function to decrease the

difference between the inverted acoustic impedance and the synthetic acoustic impedance, Cui and Hoffman were able to calibrate the initial model by varying the permeability values. It was concluded that incorporation of time-lapse seismic information reduces the uncertainty associated with reservoir models and provides more information about the geology and behavior of the formation. It was not possible to create a model that matches the real data exactly because there were numerous factors contributing to the seismic responses, and matching process was implemented by perturbing only one property. However, history matching with the time-lapse seismic information helped reduce uncertainties associated with flow modeling and rock physics modeling and provides important geologic information.

2.4 SOUTHEAST REGIONAL CARBON SEQUESTRATION PARTNERSHIP (SECARB)

As a part of the Regional Carbon Sequestration Partnership Program supported by the U.S. Department of Energy and the National Energy Technology Laboratory, the Southeast Regional Carbon Sequestration Partnership (SECARB) is a $34 million project aimed at designing sequestration and monitoring techniques for long-term carbon storage using Cranfield Field in Mississippi as the test field site. The Gulf of Coast Carbon Center (GCCC) of Bureau of Economic Geology in collaboration with Denbury Resources, Sandia Technologies, Schlumberger Carbon Services, Lawrence Berkeley National Lab, and University of Mississippi are the partners on this project. The project began in 2003 and more than 3 million metric tons of CO_2 has been injected at Cranfield Field since July 2008 (Hovorka, 2013). The main focus of the GCCC is on geologic characterization of the field, fluid-flow modeling, and development of monitoring techniques and strategies using time-lapse seismic data.

Out of hundreds of potential fields for carbon sequestration and CO_2 EOR in the Gulf Coast area (Holtz et al., 2005), Cranfield was selected as the study site based on its favorable geology and cost and legal issues (Hovorka, 2013). Cranfield is a salt-cored dome structure located in the Mississippi salt basin (Figure 2-2). It receives CO_2 from Jackson Dome field through a 160-km long pipeline (Lu et al., 2013).

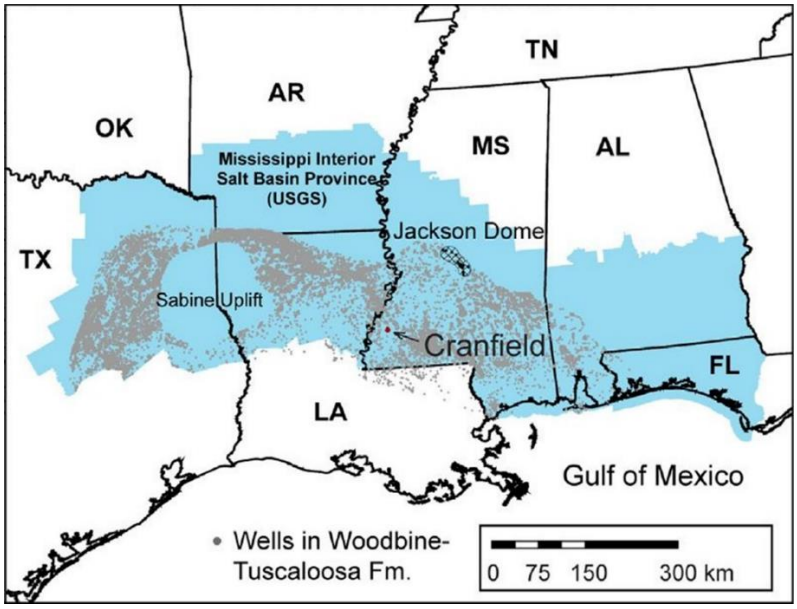

Figure 2-2: Cranfield Field located in the Mississippi salt basin. More than 3 million metric tons of CO_2 has been injected since 2008, sourced from Jackson Dome field via 160-km pipeline (Lu et al., 2013).

2.4.1 Geology of Cranfield Field

CO_2 is injected into the Lower Tuscaloosa Formation about 3200m deep. The Lower Tuscaloosa Formation was deposited during the Upper Cretaceous period as a fluvial-deltaic depositional system in the transgressive stage of the depositional cycle (Berg and Cook, 1962; Spooner Jr., 1964). The reservoir is siliciclastic with quartz being the dominant mineral. The reservoir sits on top of the Washita Group and below the Austin-Selma Group (Carter, 2014; Kordi, 2013; Lu et al., 2013). As shown in Table 2-1, the

Selma-Austin Group in the Upper Cretaceous is composed of chalk and marl. Within the Upper Cretaceous Tuscaloosa Group are three formations: Upper, Middle, and Lower Tuscaloosa sandstone. The Middle Tuscaloosa shale forms a cap rock above the Lower Tuscaloosa sandstones.

ERA	SERIES	GROUP/FORMATION		LITHOLOGY
Cretaceous	Upper	Selma-Austin		Chalk and Marl
		Tuscaloosa	Upper	Silty Sandstone
			Middle	Shale/Mudstone
			Lower	Sandstone
	Lower	Washita		Shale/Mudstone

Table 2-1: Generalized stratigraphic column of the Cranfield reservoir. The injection interval is located in the siliciclastic Lower Tuscaloosa Formation confined by the Middle Tuscaloosa shale that forms the caprock (Carter, 2014; Kordi, 2013; Lu et al., 2013).

The reservoir model for this thesis is created based on the reservoir conditions of the Designed Area of Study (DAS) specified by the GCCC. Located 12 miles east of Natchez, MS, the 25m-thick amalgamated fluvial sandstone reservoir is located in the Upper Cretaceous Lower Tuscaloosa Formation at a depth that varies from 3178m to 3207m, with a dip angle of about 2^{o} (Delshad et al., 2013; Hosseini et al., 2013; Kordi, 2013; Lu et al., 2011). One injection well (CFU 31F-1) and two observatory wells (CFU 31F-2 and CFU 31F-3) are drilled within a spacing of 100m as shown in Figure 2-3 (Ajo-Franklin et al., 2013). Hundreds of core samples have been extracted from two observatory wells and petrophysical properties such as porosity, permeability, and lithology have been

determined (Lu et al., 2013). The observation wells have been used to monitor the migration of CO_2 and the changing water saturation.

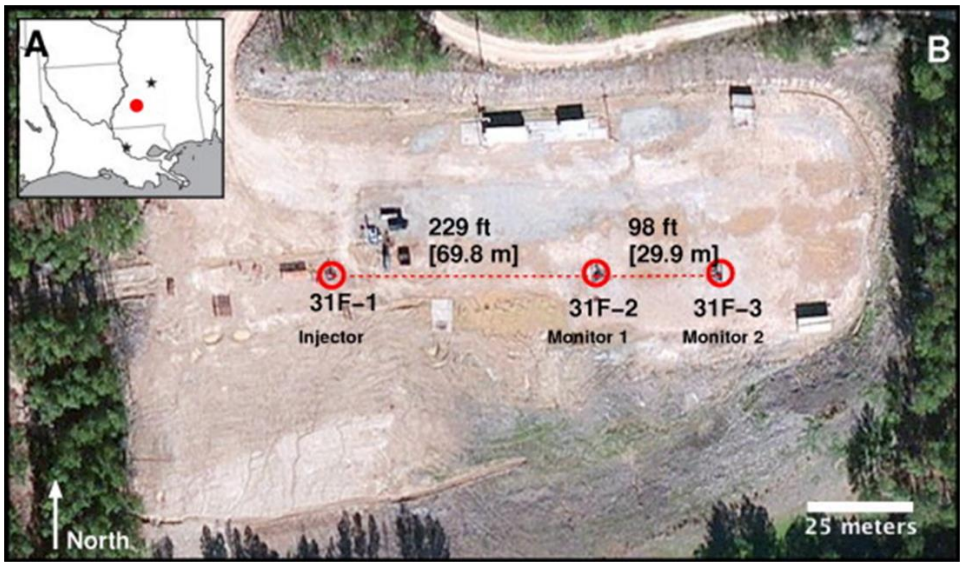

Figure 2-3: Designed Area of Study (DAS) in the Cranfield Site located 12 miles east of Natchez, MS. CO_2 is injected through the injector 31F-1 into the Upper Cretaceous Lower Tuscaloosa Formation. The migration of the injected CO_2 and the reservoir response is observed at two observatory wells 31F-2 and 31F-3 (Ajo-Franklin et al., 2013).

2.4.2 Cranfield Reservoir Characterization

In order to characterize the Tuscaloosa formation at the Cranfield site, geology reports from Spooner (1964) and Berg and Cook (1962) were first examined (Lu et al., 2013). Berg and Cook found that quartz was the dominant mineral, followed by calcite cement. The actual mineral composition in the reservoir was recently assessed using core samples by Lu et al. (2012). They discovered that the rocks contained considerable amount of clay (chlorite and kaolinite) in the DAS area in addition to quartz and calcite cement. They also experimentally examined the geochemical effects of carbonates (calcite and

dolomite), which make up 1.5% of the reservoir in the DAS. The following reactions were examined (equations 2.17 and 2.18).

$$\overbrace{CaCO_3}^{calcite} + CO_2 + H_2O \rightarrow Ca^{2+} + 2HCO_3^- \quad \text{.....(2.17)}$$

$$\overbrace{CaMg(CO_3)_2}^{dolomite} + 2CO_2 + 2H_2O \rightarrow Ca^{2+} + Mg^{2+} + 4HCO_3^- \quad \text{.....(2.18)}$$

From dissolution of carbonates, they estimated that 147 mg/L of Ca and 30 mg/L of Mg were released from the mineral samples. These effects were concluded "insignificant," in terms of mineral trapping. The goal in this thesis is to quantify the effects in petrophysical terms and then to assess whether these geochemical alterations could be assessed using seismic information.

In addition, time-lapse seismic survey data plays a key role in the SECARB project (Ajo-Franklin et al., 2013; Carrigan et al., 2013; Doetsch et al., 2013; Zhang et al., 2013). Because the Lower Tuscaloosa sandstone is a relatively thin-bedded reservoir, it is difficult to capture the details of the reservoir structure using seismic information. Zhang et al. (2013) used basis pursuit inversion to enhance the details observed in the seismic datasets and detected CO_2 plume migration at different time steps that matched well with the log data. Carter and Spikes (2013) applied rock physics models such as Gassmann fluid substitution, contact cement model, and Hertz-Mindlin theory to the inverted data to develop methods to predict mineral composition in the reservoir and to perform sensitivity analysis of CO_2 saturation in the DAS.

2.5 SUMMARY

The literature review of past experimental and simulation works on geochemistry of CO_2 injection into aquifers reveal that geochemical reactions are complex and are challenging to model. It is difficult to assess the impact of reactions on the seismic response

due to absence of a rock physics model that explicitly accounts for reactions. In this work, the combination of a numerical compositional simulator and rock physics model is used to investigate the impact of alterations in rock properties on the time-lapse seismic response. The unique model selection methodology presented in this paper is efficient at detecting the important features in the seismic and injection response that is induced by the geochemical alterations occurring in the reservoir. The results of this time-lapse study can provide new interpretation of events observed in time-lapse seismic data that might lead to a better assessment of leakage pathways and other risks.

Chapter 3: Methods Used

The only data available to model the reservoir are the well log data at three well locations and time-lapse seismic data. With very limited information, geostatistical methods are required to statistically generate reservoir models. Subsequently, reactive transport simulation and rock physics modeling were required to compute the corresponding time-lapse seismic responses. Subsequently, a model selection and expansion procedure was implemented to refine the models and select the subset of models that reflect the observed time-lapse seismic data. The basics of these techniques are introduced in this chapter.

3.1 Reservoir Characterization using Geostatistical Methods

Spatial estimation or interpolation is one of the primary aspects of geostatistics. Unlike linear regression where an outcome is estimated using a weighted linear combination of the available data, where the weights are a function of the correlation between the data and the unknown, in geostatistical methods, the redundancy between the data is also considered when computing the weights. Thus, the correlation between the data and the unsampled location as well as the correlation between the data themselves are considered in geostatistical methods for spatial interpolation or estimation. In order to facilitate the quantification of uncertainty, spatial estimation is extended to spatial simulation using techniques such as sequential Gaussian simulation and sequential indicator simulation (Chilès and Delfiner, 2012). When well data is applied to these methods, multiple number of reservoir models are statistically generated. With the limitations in acquiring necessary data, it is often difficult to objectively assess if any one model will provide accurate predictions of reservoir performance. It is important to study

behaviors of all the models and quantify the resultant uncertainty in performance prediction.

Geostatistical modeling begins with creating an experimental semivariogram, which is a measure of the spatial variability of the particular reservoir attribute under study. The variogram, γ, is expressed as in equation 3.1.

$$2\gamma(\underline{u},\underline{u}+\underline{h}) = E\left\{\left(Z(\underline{u}) - Z(\underline{u}+\underline{h})\right)^2\right\}, \quad (3.1)$$

where $Z(\underline{u})$ and $Z(\underline{u}+\underline{h})$ are the random function variables at the location $\underline{u}$ and at the lag distance, $\underline{h}$, away from $\underline{u}$, respectively. Inference of this statistics requires invoking a decision of stationarity that enables data to be pooled over all pairs that are separated by a similar lag $\underline{h}$. The experimental variogram may, in most cases be noisy due to the lack of data and needs to be modeled using positive-definite variogram models such as the spherical, exponential, or Gaussian models (Isaaks and Srivasatava, 1989). The model used in the thesis is Gaussian and spherical, which are shown in Equations 3.2 and 3.3.

$$\gamma(\underline{h}) = 1 - e^{-3\left(\frac{|\underline{h}|}{a}\right)^2}, \quad (3.2)$$

$$\gamma(\underline{h}) = \frac{3}{2}\left(\frac{h}{a}\right) - \frac{1}{2}\left(\frac{h}{a}\right)^3, \quad (3.3)$$

where a is the range of continuity. After the variogram is modeled, Kriging (Chilès and Delfiner, 2012)an be used to obtain an unbiased estimate of a variable, Z^*, (Equation 3.4) as a linear combination of the available data $Z(u_\alpha)$ with weights, λ, that minimize error variance (Equation 3.5).

$$Z^*(\underline{u}) = \sum_{\alpha}^{n} \lambda_\alpha Z(\underline{u}_\alpha) \quad (3.4)$$

$$E\left\{\left(Z(\underline{u}) - Z^*(\underline{u})\right)^2\right\} \quad (3.5)$$

The process of minimizing the error variance results in the following system of equations (Equation 3.6) that together with the unbiasedness condition (Equation 3.7) can be solved to compute the weights:

$$E\left\{\left(Z-Z^*\right)^2\right\}=\sum_{\alpha}\sum_{\beta}\lambda_\alpha\lambda_\beta Cov\left(\underline{h}_{\alpha\beta}\right)-2\sum_{\alpha}\lambda_\alpha Cov\left(\underline{h}_{\alpha 0}\right)+Cov\left(\underline{h}_{00}\right),$$

$$\frac{\partial}{\partial\lambda_\alpha}E\left\{\left(Z-Z^*\right)^2\right\}=2\sum_{\beta}\lambda_\beta Cov\left(\underline{h}_{\alpha\beta}\right)+2Cov\left(\underline{h}_{00}\right)=0,$$

$$\sum_{\beta}\lambda_\beta Cov\left(\underline{h}_{\alpha\beta}\right)=Cov\left(\underline{h}_{\alpha 0}\right),$$

……..…….....(3.6)

$$E\left(Z\mid Z^*\right)=Z^*$$ ……..……..……..…….(3.7)

If the data follows a Gaussian distribution, sequential Gaussian simulation can be used to preserve the spatial continuity of the reservoir model and also to quantify the uncertainty due to sparse data (Chilès and Delfiner, 2012). During sequential Gaussian simulation, a random path is generated visiting each of the unsampled locations in the reservoir. At the first node on the path, Kriging is performed to obtain an estimate, that according to the theory of Gaussian RVs is the mean of the conditional distribution at that location. The conditional variance is equated to the kriging estimation variance given by Equation 3.8:

$$\sigma_K^2=Cov\left(\underline{h}_{00}\right)-\sum_{\alpha}\lambda_\alpha Cov\left(\underline{h}_{\alpha 0}\right)$$ ……..……(3.8)

The mean and variance computed using Kriging are sufficient to characterize the conditional distribution at that location. A value is simulated at the location by randomly sampling the conditional distribution. The simulated value is now treated as an additional hard data, and the simulation proceeds to the next node along the random path. The process repeats until a complete reservoir model is generated.

One of the disadvantage of using sequential Gaussian simulation is that the data must follow the Gaussian distribution. Sequential indicator simulation does not require a normality assumption and works with the non-parametric distribution, $F(\underline{u};z_k)$ obtained by indicator coding the available data (Chilès and Delfiner, 2012). The simulation involves indicator variable, $I(\underline{u};z_k)$ corresponding to thresholds, z_k, as defined below:

$$I\left(\underline{u};z_k\right)=\begin{cases}1, \text{if } Z\left(\underline{u}\right)\le z_k\\ 0, \text{otherwise}\end{cases} \qquad \text{……..…..…..…..…..…(3.9)}$$

$$E\left\{I\left(\underline{u};z_k\right)\right\}=\text{Prob}\left\{Z\left(\underline{u}\right)\le z_k\right\}=F\left(\underline{u};z_k\right)$$

Indicator kriging is interpreted as the process of updating the prior uncertainty $F(\underline{u};z_k)$ to the posterior uncertainty $F^*(\underline{u}|(n))$ as given by Equation 3.10.

$$F^*\left(\underline{u};z_k\,|\,(n)\right)=\left[1-\sum_{\alpha=1}^{n}\lambda_\alpha\left(u;z_k\right)\right]F\left(Z_k\right)+\sum_{\alpha=1}^{n}\lambda_\alpha\left(u;z_k\right)I\left(u;z_k\right) \text{……..…..…(3.10)}$$

As in sequential Gaussian simulation, a random path is generated through the unsampled locations in the reservoir. Instead of drawing a value based on the Gaussian distribution of the hard data, the non-parametric conditional probability $F^*(\underline{u}|(n))$ is used to simulate a value at each node on the path, which is then added to the conditioning data set. The process is repeated until the entire path is visited.

3.2 REACTIVE TRANSPORT SIMULATION

CMG-GEM (Computer Modelling Group Ltd., 2013) is a commercial geochemical equation-of-state (EOS) compositional simulator that is capable of modeling transport of fluids and chemical species in porous media with accompanying mineral reactions. Ngheim et al. (2004) simulated carbon sequestration in a reservoir that has very similar conditions as the one at Cranfield using CMG-GEM. The details on reaction stoichiometry, chemical equilibrium between the aqueous solutions, material balance, and reaction rates, etc. can

be found in the paper by Ngheim et al. There are two components in the injected fluid: CO_2 and C_1. Because CMG-GEM is primarily an oil field simulator, there has to be a hydrocarbon phase and component at all time steps of the simulation. Consequently, C_1 is an insoluble trace component that does not flow but is specified in order to prevent the hydrocarbon component from disappearing. The PVT properties of the two components are shown in Table 3-1. Figure 3.1 shows the CO_2-brine relative permeability curves used in the simulation.

Table 3-1: The PVT properties of injected CO_2 and C_1. C_1 is a trace component and is assumed insoluble in water and therefore does not have an effect on geochemistry of the reservoir.

PROPERTIES	**CO_2**	**C_1**
Critical Pressure (atm)	72.80	45.40
Critical Volume (m^3/k-mol)	0.09	0.10
Critical Temperature (K)	304.20	190.60
Boiling Temperature (^oC)	-78.45	-161.45
Acentric Factor	0.23	0.01
Molecular Weight	44.01	16.04
Specific Gravity	0.82	0.30

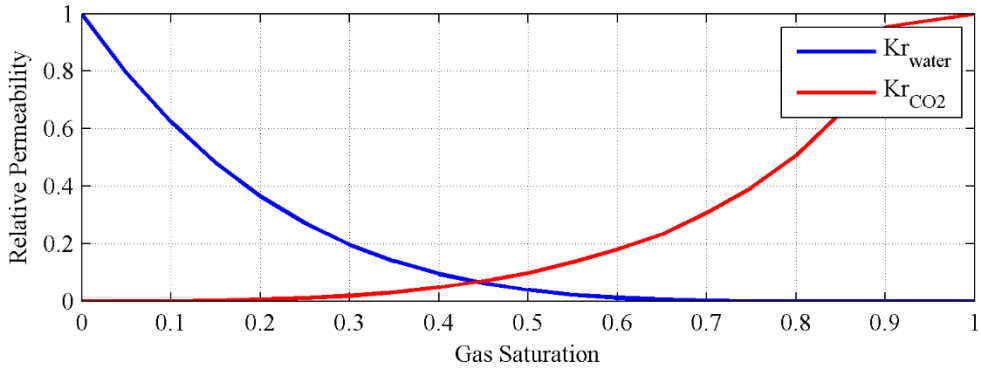

Figure 3.1: Relative permeability for CO_2 and brine used in the reactive transport simulation performed by Ngheim et al (2004).

Equations 3.11, 3.12, and 3.13 express the reactions involved in the flow and transport simulation. When CO_2 is injected, it dissolves in brine to release hydrogen and bicarbonate ions (3.1), that lowers the pH of the aquifer and initiates calcite (3.2) and dolomite (3.3) dissolution/precipitation.

$$CO_2 + H_2O \rightarrow H^+ + HCO_3^{2-} \quad \text{.....(3.11)}$$

$$\overbrace{CaCO_3}^{calcite} + H^+ \leftrightarrow Ca^{2+} + HCO_3^- \quad \text{.....(3.12)}$$

$$\overbrace{CaMg(CO_3)_2}^{dolomite} + 2H^+ \leftrightarrow Ca^{2+} + Mg^{2+} + 2(HCO_3^-) \quad \text{.....(3.13)}$$

The chemical-equilibrium constants for above reactions are -13.2631, 1.3560, and 1.6727, respectively (Nghiem et al., 2004). When a mineral is dissolved or precipitated, its molar mass changes. The molar density is then used to derive the volume change in each grid block. The ratio of the changed volume to the simulation grid block volume is the change in porosity that also induces the change in permeability computed using the Kozeny-Carmen (Computer Modeling Group Ltd., 2013). These changes in turn translate into changes in elastic properties by applying the rock physics models discussed in the next section.

3.3 ROCK PHYSICS MODELING

Rock physics models are crucial to link variations in petrophysical properties to corresponding variations in elastic properties of rocks. In this section, the models used to accomplish this, based on the general rock-physics models presented in Mavko, Mukerji, and Dvorkin (2009), cementation theory by Dvorkin and Nur (1996), and Hertz-Mindlin theory (Mindlin, 1949; Dvorkin and Nur, 1996), are presented.

The Reuss average (Reuss, 1929) is used to compute the elastic moduli of the fluid mixture, M_R, which is calculated using Equation 3.14.

$$\frac{1}{M_R} = \sum_{i=1}^{N} \frac{f_i}{M_i}, \quad \text{.....(3.14)}$$

where f_i and M_i are each fluid's volumetric concentration and elastic modulus, respectively. The Voigt-Reuss-Hill average is used to compute the elastic moduli of minerals based on their volumetric fractions, f_i. It is half the sum of the Reuss and Voigt bounds (Equations 2.15 and 2.16).

$$M_{VRH} = \frac{\overbrace{\sum_{i=1}^{N} f_i M_i}^{Voigt} + \overbrace{\left(\sum_{i=1}^{N} \frac{f_i}{M_i} \right)^{-1}}^{Reuss}}{2} \quad \text{.....(3.15)}$$

Bulk density, ρ_{bulk}, is an average of densities of each component weighted by their respective volume fractions, which can be represented in terms of porosity, ϕ, and water saturation, S_w.

$$\rho_{bulk} = (1-\phi)\rho_{mineral} + \phi(1-S_w)\rho_{CO_2} + \phi S_w \rho_{brine} \quad \text{.....(3.16)}$$

With the elastic moduli and density derived from the above equations, P-wave velocity, V_p, and S-wave velocity, V_s, can be derived using the following equations.

$$V_p = \sqrt{\frac{K + \frac{4}{3}\mu}{\rho}}\,,\; V_S = \sqrt{\frac{\mu}{\rho}}, \quad \text{.....(3.17)}$$

where the elastic moduli K and μ are calculated using the averaging schemes in Equations 3.14 and 3.15 above. A Poisson's ratio is derived in terms of P-wave and S-wave velocities as below.

$$\nu = \frac{V_P^2 - 2V_S^2}{2(V_P^2 - V_S^2)} \quad \text{.....(3.18)}$$

The cementation theory developed by Dvorkin and Nur (1996) describes a mechanical behavior of grains bound by cement. The theory considers a load-bearing cement that has a major impact on the rock stiffness. Equation 3.19 below derives the elastic moduli of the grains that are assumed to be identical and spherical with the intergranular cement in contact. The number of contacts per grain, n, and critical porosity, ϕ_0, the porosity at which grains become suspended, used in the model are approximately 9 and 0.36, respectively.

$$\begin{aligned}
K_{dry} &= \frac{1}{6} n(1-\phi_0) M_c S_n, \\
G_{dry} &= \frac{3}{5} K_{dry} + \frac{3}{20} n(1-\phi_0) G_c S_\tau; \quad \text{.....(3.19)} \\
M_c &= \rho_c V_{Pc}^2, \\
G_c &= \rho_c V_{Sc}^2;
\end{aligned}$$

where M_c and G_c are the elastic moduli of the cement; V_{Pc} and V_{Sc} are the wave velocities of the cement; and ρ_c is the cement density. S_n and S_τ are parameters that are proportional to stiffness of a grain composite. They are derived using the empirical equations below derived on the basis of laboratory measurements.

$$
\begin{aligned}
&S_n = A_n\alpha^2 + B_n\alpha + C_n,\\
&A_n = -0.024153\Lambda_n^{-1.3646},\\
&B_n = 0.20405\Lambda_n^{-0.89009},\\
&C_n = 0.00024649\Lambda_n^{-1.9846};\\
&S_\tau = A_\tau\alpha^2 + B_\tau\alpha + C_\tau,\\
&A_\tau = -10^{-2}(2.26\nu^2 + 2.07\nu + 2.3)\Lambda_\tau^{0.079\nu^2+0.1754\nu-1.342},\\
&B_\tau = (0.0573\nu^2 + 0.0937\nu + 0.202)\Lambda_\tau^{0.0274\nu^2+0.0529\nu-0.8765},\\
&C_\tau = -10^{-4}(9.654\nu^2 + 4.945\nu + 3.1)\Lambda_\tau^{0.01867\nu^2+0.4011\nu-1.8186};\\
&\Lambda_n = \frac{2G_c}{\pi G_g}\frac{(1-\nu_g)(1-\nu_c)}{1-2\nu_c},\\
&\Lambda_\tau = s\frac{G_c}{\pi G_g},
\end{aligned}
$$

……..……(3.20)

where G_g and G_c are the shear moduli of grains and of cement, respectively; and ν_g and ν_c are the Poisson's ratios of grains and of cement. The terms A, B, C, and Λ are used to statistically solve for S_n and S_τ and do not have physical meanings. α, a unitless parameter, describes the amount of cement in contact with grains. With the assumption that the cement is localized on grain contacts, the below equation is used for finding α.

$$\alpha = 2\left(\frac{\phi_0 - \phi}{3n(1-\phi_0)}\right)^{0.25} \quad \text{……..……(3.21)}$$

The Hertz-Mindlin theory (Mindlin, 1949; Dvorkin and Nur, 1996) applies modified Hashin-Shtrikman bound (Hashin and Shtrikman, 1963) to predict the elastic moduli of a dry rock near critical porosity, the porosity at which grains become suspended. The model is useful for poorly consolidated formations. The following set of equations (3.22) expresses the elastic moduli of the rock at a pressure P and at a critical porosity ϕ_0. The same notations as the ones in previous equations are used.

$$K_{HM} = \left(\frac{n^2 (1-\phi_0)^2 G_g{}^2}{18\pi^2 (1-\nu)^2} P \right)^{\frac{1}{3}},$$

$$G_{HM} = \frac{5-4\nu}{5(2-\nu)} \left(\frac{3n^2 (1-\phi_0)^2 G_g{}^2}{2\pi^2 (1-\nu_g)^2} P \right)^{\frac{1}{3}} \quad \text{.....(3.22)}$$

When CO_2 is injected and causes mineral reactions, porosity will change. We need to be able to obtain the elastic moduli of a dry rock at any porosity ϕ. The following equations are used for this case (Mindlin, 1949; Dvorkin and Nur, 1996):

$$K_{dry} = \left(\frac{\frac{\phi}{\phi_0}}{K_{HM} + \frac{4}{3} G_{HM}} + \frac{1-\frac{\phi}{\phi_0}}{K_g + \frac{4}{3} G_{HM}} \right)^{-1} - \frac{4}{3} G_{HM}$$

$$G_{dry} = \left(\frac{\frac{\phi}{\phi_0}}{G_{HM} + \frac{G_{HM}}{6} \left(\frac{9K_{HM} + 8G_{HM}}{K_{HM} + 2G_{HM}} \right)} + \frac{1-\frac{\phi}{\phi_0}}{G_g + \frac{G_{HM}}{6} \left(\frac{9K_{HM} + 8G_{HM}}{K_{HM} + 2G_{HM}} \right)} \right)^{-1}$$

$$- \frac{G_{HM}}{6} \left(\frac{9K_{HM} + 8G_{HM}}{K_{HM} + 2G_{HM}} \right)$$

……(3.23)

As mentioned in Chapter 2, these models are appropriate for high-frequency description of rock properties. In order to apply these models for low frequency (100s of Hz) description of reservoir rock, the elastic moduli of the dry rock frame should be derived (Mavko et al., 2009). Gassmann's theory (Gassmann, 1951) is used to perform fluid substitution and to compute bulk modulus of the saturated rock. In Gassmann's theory, shear modulus of the saturated rock is not effected by fluid saturation and therefore remains the same as the one in the dry rock, but the bulk modulus is affected by the fluid saturation.

$$K_{sat} = K_{dry} + \frac{\left(1 - \frac{K_{dry}}{K_0}\right)^2}{\frac{\phi}{K_{fl}} + \frac{(1-\phi)}{K_0} - \frac{K_{dry}}{K_0^2}},$$

$$G_{sat} = G_{dry},$$

……...……...……(3.24)

where K_{sat}, K_{dry}, and K_0 are the bulk moduli of the saturated rock, dry rock, and mineral, respectively; and G_{sat} and G_{dry} are the shear moduli of the saturated rock and dry rock, respectively. The elastic moduli are then applied to Equation 3.17 to derive elastic wave velocities of the reservoir.

3.4 FORWARD SEISMIC MODELING

Forward seismic modeling allows us to visualize spatial variations in reservoir properties. The seismic signature is modeled by convolving reflection coefficient, $R_0(t)$, with a wavelet, w(t), and subsequently adding a noise, n(t) (Equation 3.25). In this research, the noise, $n(t)$, was neglected in the forward seismic modeling and consequently, it is assumed that the seismic signature is solely affected by the reservoir heterogeneity.

$$T(t) = R_0(t) * w(t) + n(t) \quad \text{……...……(3.25)}$$

Reflection coefficient, R_0, is the ratio of the difference in acoustic impedances (product of P-wave velocity and density derived from rock physics modeling) between two adjacent layers to the sum of acoustic impedances in the layers (Equation (3.26).

$$R_0(t) = \frac{\rho_2 V_{P2} - \rho_1 V_{P1}}{\rho_2 V_{P2} + \rho_1 V_{P1}} \quad \text{……..(3.26)}$$

The variables (densities and P-wave velocities) in the equation are assumed available in the time domain. In case the rock physics parameters are available at some depths, we can

get the equivalent time by dividing the depth by P-wave velocity and multiplying by 2 in order to obtain a two-way travel time, or *t*.

In this research, the wavelet used to generate the forward seismic response is the zero-phase Ricker wavelet with a central peak and two small lobes. It is expressed in terms of frequency, *f*, and time, *t*, as shown in equation 3.27 (Ryan, 1994).

$$w(t) = (1 - 2\pi^2 f^2 t^2) e^{-\pi^2 f^2 t^2} \quad \text{.....(3.27)}$$

3.4.1 Convolution Example

Figure 3-2 shows a simple example of deriving the seismic trace in Panel (d). Equation 3.26 is used to compute the reflection coefficient in Panel (b) using the given acoustic impedance in Panel (a). Equation 3.27 is used to create a Ricker Wavelet with a frequency of 500Hz as shown in Panel (c). Finally, Equation 3.25 is used to convolve the computed reflection coefficient with the Ricker wavelet to generate a seismic trace.

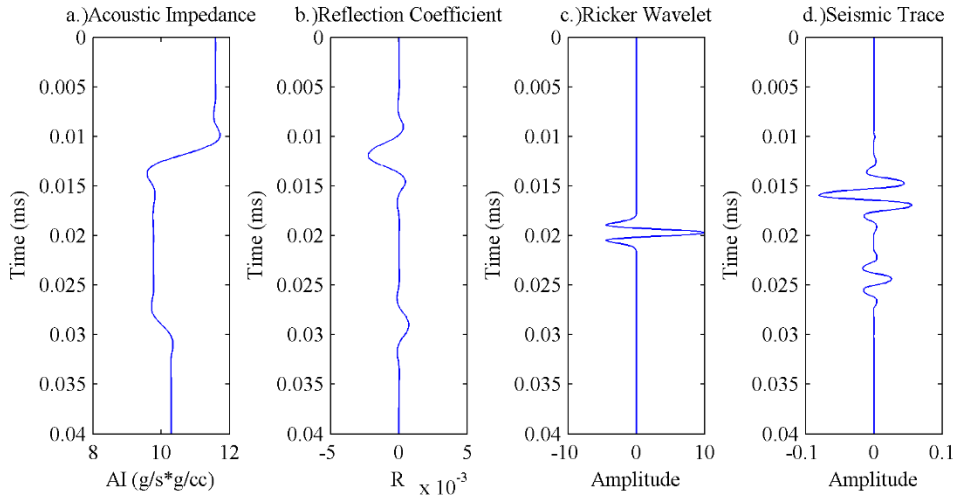

Figure 3-2: The example of the seismic trace derivation. Given (a) the acoustic impedance, (b) the reflection coefficient is computed and convolved with (c) the Ricker wavelet to obtain (d) the seismic trace.

3.5 Model Selection and Expansion

The model selection and expansion can be utilized to reduce uncertainties in models created with very limited information. An initial suite of models is statistically generated conditioned to limited information. These models are then processed through a transfer function in order to yield a response that can be compared to the actual data that is available. Those models are then compared and clustered based on their similarities with the actual data. The best models in a cluster are then randomly resampled in order to obtain additional conditioning data that are used to generate a posterior set of models. Repeating this with subsequent time lapse data can yield the models with reduced uncertainties.

In a case where a time-lapse data is available, the models in the posterior set can be used to perform numerical simulations, in order to yield the behaviors at each time step that the data is available. The simulated results are compared with the actual data in the first time step, and the models are clustered based on as the similarity of their response to the actual data. The models in the first cluster are then resampled to generate another posterior set of models. After running another set of simulations and comparing the results in the subsequent time step, the models are again clustered and resampled to generate an additional posterior set of models. This refining process repeats until all the models in the posterior set are compared with the actual data at all the time steps. The best selected models are then used for an assessment of the impact of geochemical reactions on CO2 leakage through pathways.

3.6 Statistical Measures of Similarity

3.6.1 Discrete Fréchet Distance

The Fréchet distance (Fréchet, 1906) is a measure of dissimilarity between two profiles. The Fréchet distance calculated between seismic traces or impedance profiles of

geostatistically generated reservoir models and those of the reference model sets a criteria for discriminating between models on the basis of their common characteristics. In order to understand this concept, consider a man walking a dog with a leash (Buchin et al., 2013). The man and the dog each have their own curved path and move at their own speed, but each can only go forward. The Fréchet distance is then the measure of the minimum length of a leash that the man needs.

Alt and Godau (1992) defined two curved paths as f : [a, a']→V and g : [b, b']→V, whose Fréchet distance $\delta_F(f,g)$ is defined using Equation 3.28.

$$\delta_F(f,g) = \inf_{\alpha,\beta} \max_{t\in[0,1]} \left[d\left(f(\alpha(t)), g(\beta(t)) \right) \right], \quad \text{.....(3.28)}$$

where α and β are continuingly increasing functions that map [0, 1] onto [a, a'] and [b, b'], respectively.

Eiter and Mannila (1994) have further developed the concept to derive the discrete Fréchet distance by assuming that the curved paths are polygonal curves, P:[0, n]→V and Q:[0, n]→V, where n is a positive integer. The corresponding sequence of the coupling are denoted as

$$(u_{a1}, v_{b1}), (u_{a2}, v_{b2}), ..., (u_{an}, v_{bn}) \quad \text{.....(3.29)}$$

The discrete Fréchet distance, $\delta_F(f,g)$, is the minimum of the lengths between u_{ai} and v_{bi} and is defined as

$$\delta_{dF}(P,Q) = min\left\{ \max_{i=1,...,n} \left[d(u_{ai}, v_{bi}) \right] \right\}. \quad \text{.....(3.30)}$$

3.6.2 Discrete Fréchet Distance Example

This section presents a simple example of using the discrete Fréchet distance to quantify the similarities between two curves P and Q in Figure 3-3. P and Q are created by

connecting the points as shown in the figure. Moving from x=1 to x=10, each node on one lines is coupled with the corresponding node on the other line according to its sequence as shown in Equation 3.29. The discrete Fréchet distance is then calculated using Equation 3.30. The distance between each couple ranges from 0.5 to 2.6. The maximum difference in distances is thus 2.6. This distance is comparable to the maximum distance that a man will be away from his dog. Therefore, a minimum length of a leash that he requires, or the discrete Fréchet distance, is 2.6.

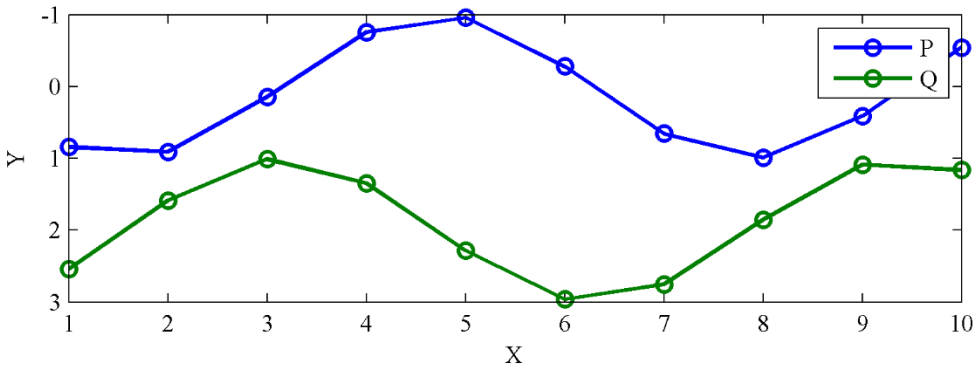

Figure 3-3: The lines used to show an example of quantifying the similarities between two curves using the discrete Fréchet distance. The discrete Fréchet distance of two curves P and Q is 2.6.

3.7 SUMMARY

When limited data is available, there is significant uncertainty associated with the reservoir model. Consequently, a unique workflow is required to integrate additional data and reduce the uncertainty associated with the geologic models. Geostatistical methods are used to statistically generate multiple models. Flow and transport simulation and rock physics modeling were utilized to transform those reservoir models into the corresponding seismic response that were compared with the available seismic data. Through the model selection and expansion techniques, the models were constantly refined to reduce the

uncertainties, and the best models were selected for investigating the behaviors of the reservoir due to long-term sequestration of the CO_2. In Chapter 4, this work flow is implemented using synthetic reference models for validation. It was then applied to the real data in Chapter 5 for a complete assessment of carbon sequestration in Cranfield and the accompanying geochemical alterations in the long term and the risks associated with it.

Chapter 4: Modeling and Monitoring the Migration of CO_2 in the Reference Model and Implementation of the Model Selection Process

Model selection is a useful tool to refine a prior set of reservoir models and reflect the posterior uncertainty after the data assimilation process. Through model selection and expansion, a subset of initial models generated using various schemes is clustered and subsequently, a group is selected and additional reservoir models are "spawned" that share the characteristics of the selected cluster. This process thus yields the posterior uncertainty that can be considered for assessing the reservoirs' response to the injected fluid. In the first half of this chapter, a set of reservoir models was created based on the well logs and reservoir properties of the Designed Area of Study (DAS) at Cranfield using geostatistical methods. One of the models was defined as "reference model" and its response to the CO_2 injection was studied. In the latter part of the chapter, the response of all generated models were investigated and refined based on their resemblance to the reference model. Although uncertainty in flow and seismic response may arise due to various factors, the main focus of this work is only to assess the uncertainty due to carbonates rock proportion in the reservoir. It is conjectured that implementation of the model selection process will help us bracket the uncertainty in the proportion of the carbonates such that the actual carbonate proportion of the reference is contained within the interval. Representing the carbonate proportion in the reservoir is important in order to assess the geochemical response of the CO_2-injected reservoir.

4.1 Modeling and Monitoring of CO_2-Rock Interactions in the Reference Model

4.1.1 Reservoir Characterization

In the Designed Area of Study (DAS) there are three wells as shown in Figure 2-4. Mineralogy data based on quantitative log analysis is only available for the well 31F-2.

The dominant mineral in the reservoir is quartz that makes up 79.4% of the rock volume, followed by clay (chlorite and kaolinite) that make up 14.8% of the rock volume. The major reactive minerals in the reservoir are calcite and dolomite, that make up only 1.5% of the reservoir (Lu et al., 2012). It is essential to determine where in the reservoir these carbonates (calcite and dolomite) facies are present. To do so, the following indicator coding of data is proposed. If carbonate facies is present at a location then an indicator code of "1" was specified and "0" if not (Table 4-1).

Table 4-1: Mineralogy of the DAS at well 31F-2. Indicator code was specified on the basis of carbonate facies proportion.

Depth (m)	**Quartz (%)**	**Clay (%)**	**Carbonates (%)**	**Carbonates Indicator**
3178.1	77.9	16.1	0.5	1
3178.9	73.7	18.1		0
3179.8	66.9	5.1		0
3191.2	75.6	2.5		0
3191.5	77.9	18.1		0
3193.2	55.2	5.9	36.8	1
3193.6	84.6	11.8		0
3193.9	81.4	15.0		0
3194.2	85.5	11.2	0.5	1
3194.9	85.1	12.3		0
3195.6	85.7	11.2	0.6	1
3195.9	80.8	16.1		0
3196.1	82.0	15.3		0
3196.8	81.9	14.7		0
3197.7	83.6	12.2	0.5	1
3199.7	71.2	15.4	9.8	1
3200.3	70.5	17.8	6.5	1

In order to perform sequential indicator simulation using the indicator data, a two-dimensional reservoir grid covering 120-meters in width and 30-meter in height was created using SGeMS. This small dimension may not be resolvable by seismic data, but

the work in this chapter was performed to examine if the geochemical alterations due to mineral reactions were visible in the scale that was slightly finer than the common resolution of seismic data. The grid covers the DAS horizontally from 10m west of 31F-1 to 10m east of 31F-3 and vertically from a depth 3175m to 3205m. The horizontal extent of the area was divided into 600 blocks, and the vertical extent into 720 blocks in order to create a very fine grid. Figure 4-1 shows one of the reservoir models created using the sequential indicator simulation with the global proportion of carbonates specified to be 1.5%, which is based on the well log data observed along well 31F-2. Red indicates regions where carbonate facies are present. The injection well (F31-1) is located at the position marked as 0m, and the two observation wells (F31-2 and F31-3) are located at 70m and 100m.

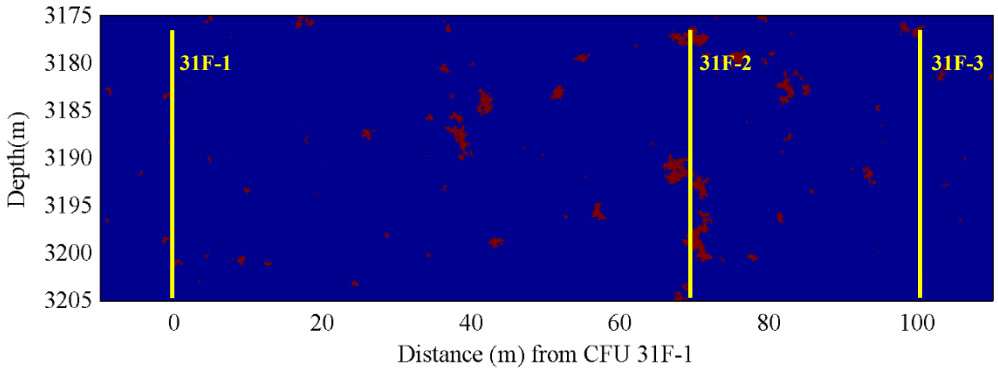

Figure 4-1: Indicator map of carbonate facies in the DAS generated using the sequential indicator simulation using the carbonates data from well 31F-2. Red indicates where carbonates are present. The carbonates make up 1.5% of the reservoir lithology.

The fine scale model was coarsened by computing the average of the indicator data in order to estimate the percentage of carbonate facies at that location of the reservoir Furthermore, a 2^{o} dip of the reservoir was simulated by specifying that the top row of grid blocks were shifted downward by the height of one smaller grid block, as shown in Figure

4-2. This process formed a new 25-by-120 reservoir grid with 1m-by-1m blocks. Within each larger block (orange), the mean of indicator data of carbonates was calculated to yield the approximate percentage of carbonates in the region. Figure 4-3 shows the reservoir with the carbonate facies proportion. This format of the model allow users to enter the data into CMG-GEM to perform flow simulations.

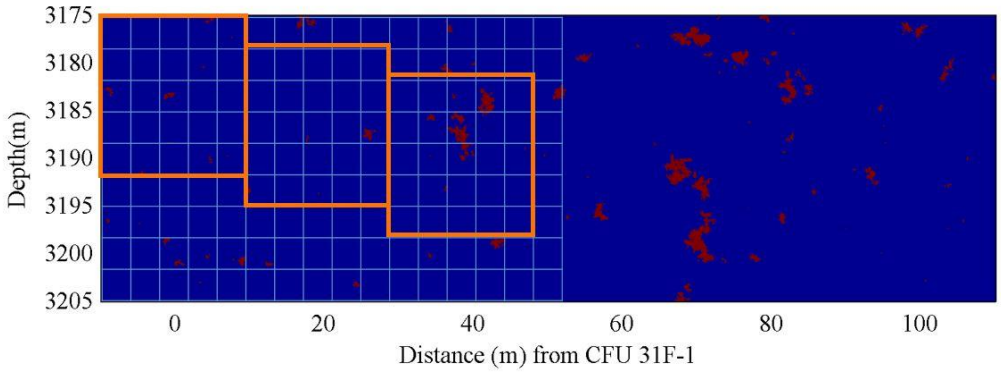

Figure 4-2: Coarsening of the fine-grid model to a new 25-by-120 reservoir grid with 1m-by-1m grid blocks (not to scale). The carbonate facies proportion within each coarse block was calculated by averaging the indicator data within the block.

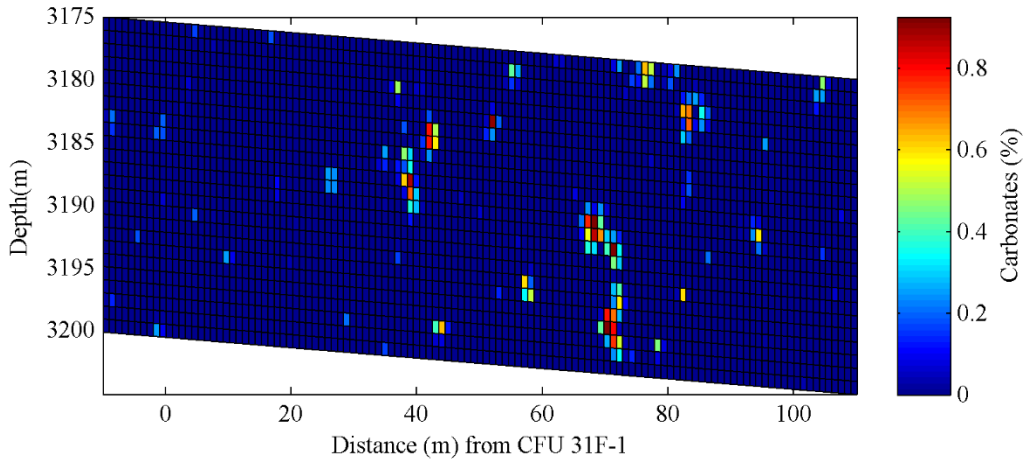

Figure 4-3: A reservoir model with the carbonates facies proportions. It was created based on the indicator map of carbonates created on a very fine grid using the sequential indicator simulation.

Porosity and permeability data are available for all three wells (Figure 4-4). Because permeability ranges from fractions to thousands of millidarcies, the logarithm transform was used. The average porosity of the reservoir is about 0.2 with higher porosity observed toward the bottom of the 31F-2 and 31F-3 wells. Both porosity and log of permeability were transformed into normal distribution while performing the sequential Gaussian simulation using SGeMS.

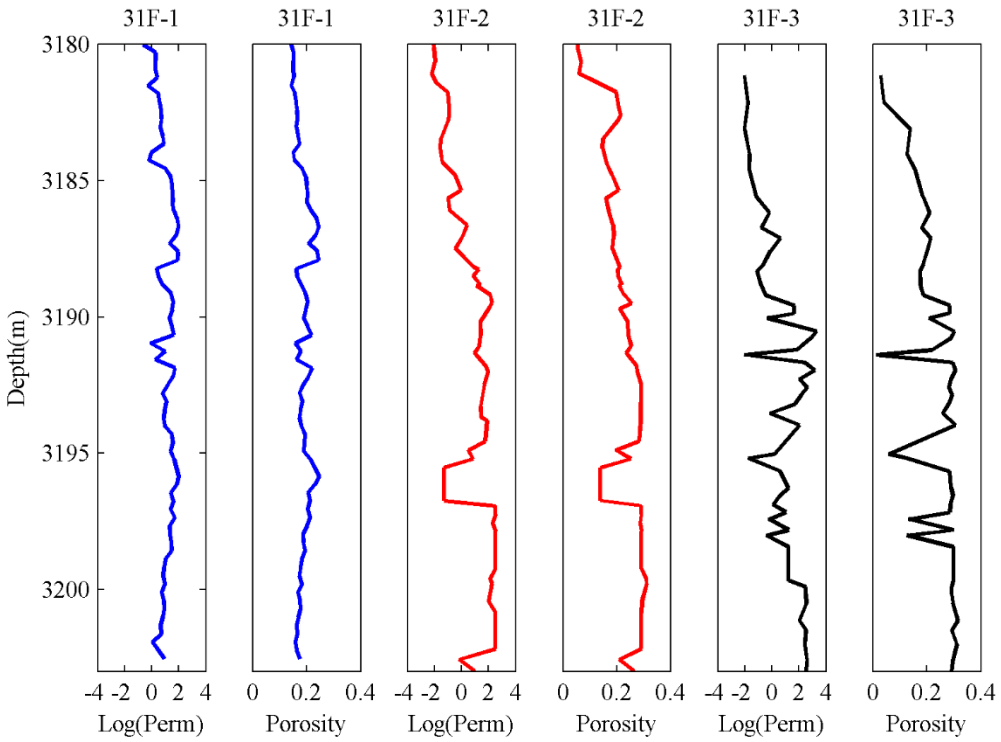

Figure 4-4: Permeability and porosity of three wells in the DAS. The logarithm of permeability was used because of the wide range of the data. Both porosity and logarithm of permeability were transformed into normal distribution prior to sequential Gaussian simulation.

Sequential Gaussian simulation was performed using the porosity and permeability data. The simulation was first performed on the fine scale 600 by 720 reservoir grid. Property variations on at the25-by-120 coarsened grid was calculated by arithmetic average and

subsequently a 2° dip was imposed on the reservoir. Figure 4-5 and 4-6 show the porosity and permeability map created for the reservoir. The permeability values were computed by back-transforming the log values.

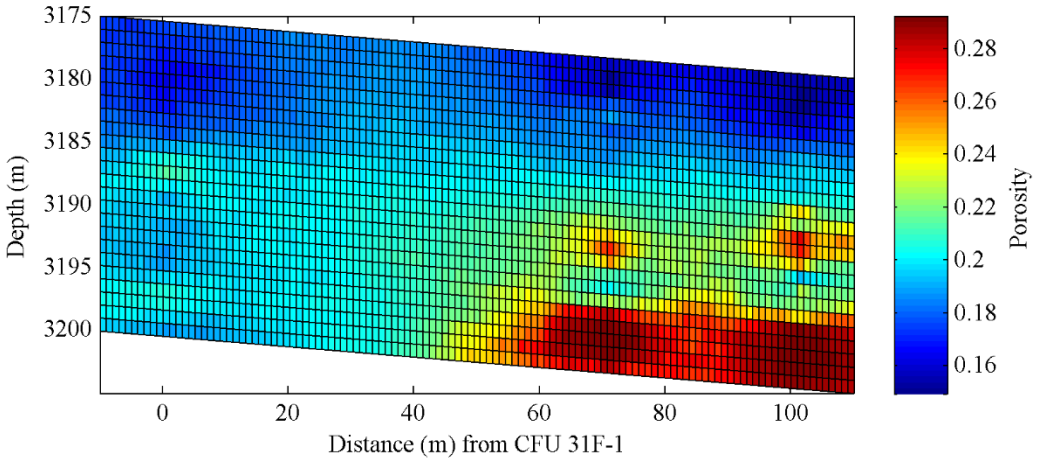

Figure 4-5: Porosity map of the DAS reservoir generated using sequential Gaussian Simulation based on the log data from the three wells. Higher porosity was observed toward the bottom east corner of the reservoir as observed in the well logs.

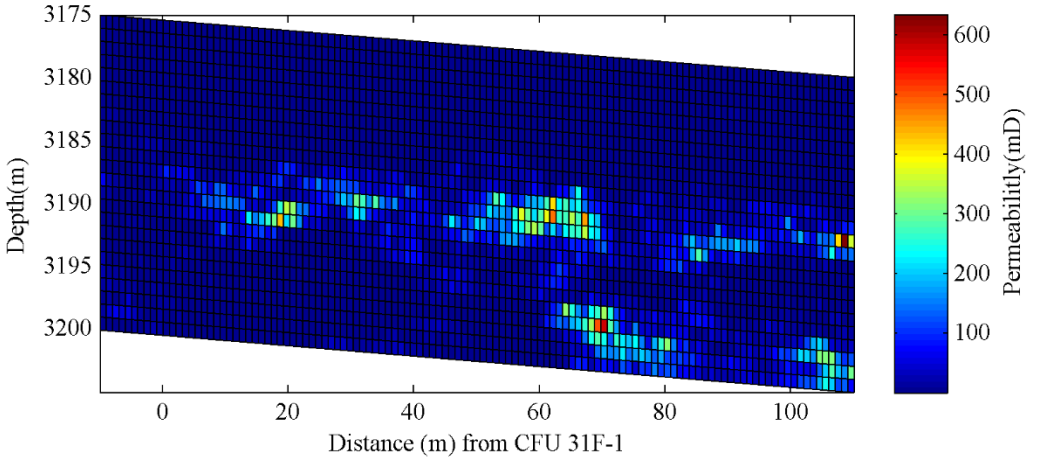

Figure 4-6: Permeability map of the DAS based on the log data from the three wells. The log of permeability was used in the sequential Gaussian simulation. The simulated values were then back-transformed in order to obtain the permeability map.

This reservoir model above with the corresponding spatial variation in carbonate facies proportion, porosity and permeability is one of several models generated using the geostatistical modeling procedure. The model detailed in this section is deemed the reference model and a work flow for deriving the seismic signature of this reservoir model, will be presented next.

4.1.2 Flow Simulation

The rock facies variation, porosity, and permeability data along with the reservoir conditions of the DAS, were entered into CMG-GEM to perform reactive-transport simulations in order to investigate the geochemical effects of CO_2 injection on reservoir properties. The conditions corresponding to an infinite reservoir were simulated because the reservoir extends far beyond the DAS. The initial pressure and temperature of the reservoir were 32MPa and 125^{o}C, respectively (Delshad et al., 2013; Hosseini et al., 2012; Kordi, 2013). The relative permeability parameters implemented by Ngheim et al. (2004) were used in the simulations. There are two carbonate facies: calcite and dolomite. According to the mineralogy along well 31F-2, the proportion of calcite is 1.1% while that of dolomite is 0.4% of dolomite (Lu et al., 2012). One pore volume of CO_2 was injected at the bottom interval of well 31F-1 over a two-year period. The behavior of the reservoir was observed for a period of 98 years after injection.

There was a change in porosity due to calcite and dolomite dissolution and precipitation. Even after injection stopped, CO_2 continued dissolving in brine to cause reactions. Figures 4-7 to 4-9 show the changes in porosity at the beginning of year 0, 50, and 100, respectively. The most change in porosity was observed after 50 years because of active reactions. When CO_2 is injected, it is intuitive to expect only the dissolution of minerals at the early stages. However, the formation brine in DAS is originally composed

of aqueous components like calcium ions (Lu et al., 2011). The presence of calcium ions caused precipitation of calcite even during the early stages of the monitoring period. A noticeable level of dissolution was observed at the top section of the reservoir. The low density of CO_2 relative to that of brine caused it to be buoyant and reactive near the top of the reservoir. Small changes in porosity were detected even after year 50 near the injection zone and at the bottom east (right) corner, indicating continuing precipitation. The high level of dissolution during the early stage, followed by continuing precipitation mimics the result that Ngheim et al. (2004) observed in their studies.

The changes in water saturation of the reservoir (Figures 4-10 to 4-12) also reflected the buoyant nature of the CO_2 plume. As CO_2 continued to migrate upward, water saturation became dominant in the lower half of the reservoir. Because of the high water saturation in the surrounding saline aquifer, water tends to encroach in order to re-saturate the reservoir.

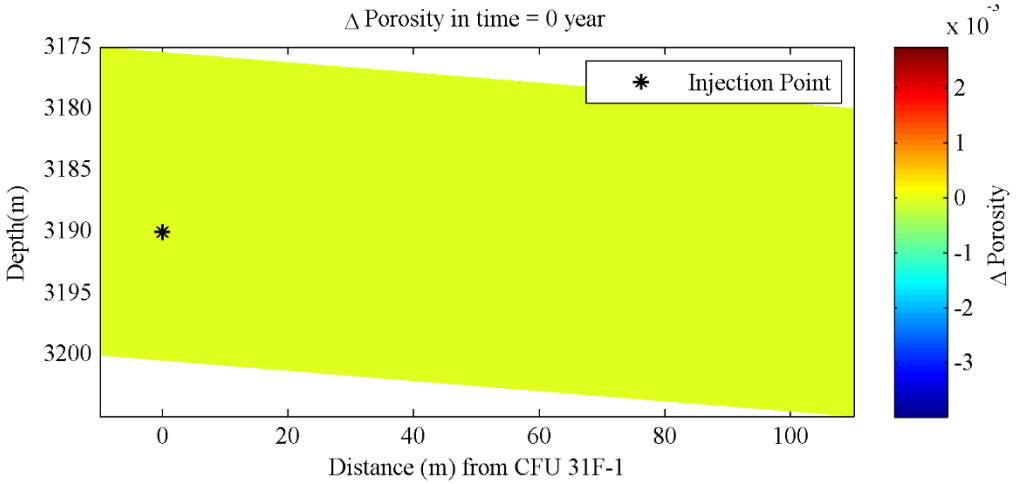

Figure 4-7: Porosity change at the start of injection. Because CO_2 had not been injected yet, the reservoir showed no change in porosity.

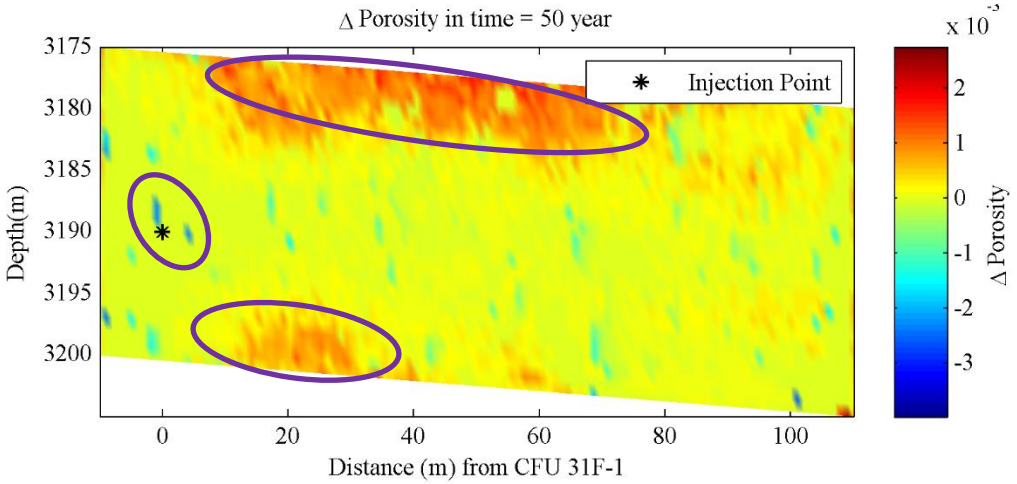

Figure 4-8: Porosity change in year 50. Decrease in porosity near the injection zone indicates that there was precipitation of the carbonates because of calcium ions originally dissolved in the brine. Dissolution of the minerals near the top of the reservoir is explained by the buoyant nature of low-density CO_2 plume traveling upward. The unexpected dissolution at the bottom of the reservoir may be due to CO_2-saturated brine in contact with the minerals during the early stage of injection before it migrated upward.

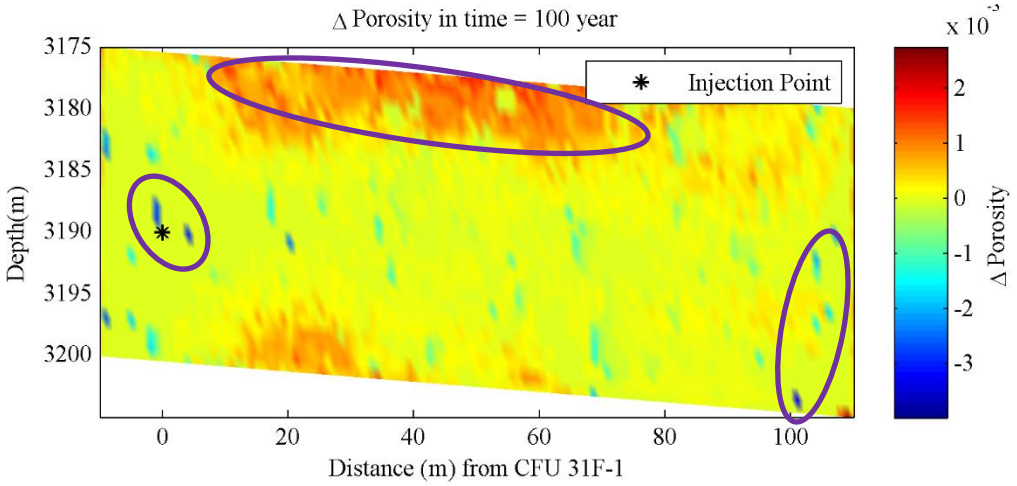

Figure 4-9: Porosity change in year 100. Although not much had been changed since year 50, precipitation of calcite near the injection zone and at the bottom east (right) corner of the reservoir was observed.

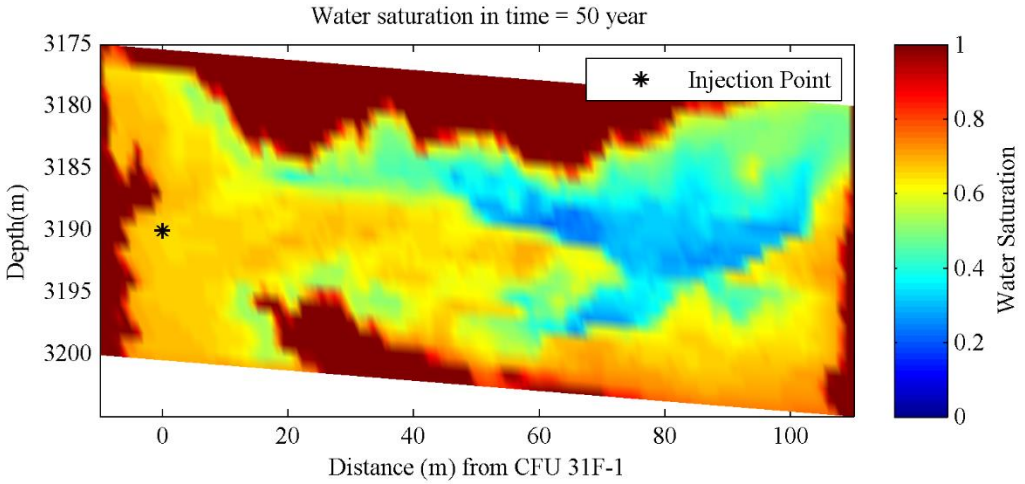

Figure 4-10: Water saturation in year 50. Because CO_2 has a lower density than brine, the gas saturation is higher near the top half of the reservoir. The irregular pocket at the top formed due to the heterogeneity in permeability that caused CO_2 to migrate upward at different rates.

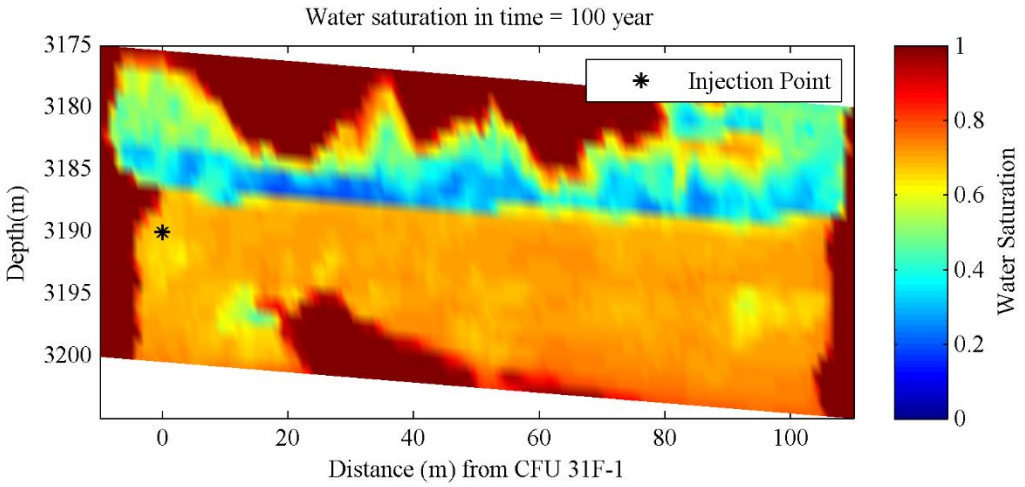

Figure 4-11: Water saturation distribution in DAS in year 100. This is 98 years after CO_2 injection was stopped. Water saturation rebounds because of encroachment of water from the periphery.

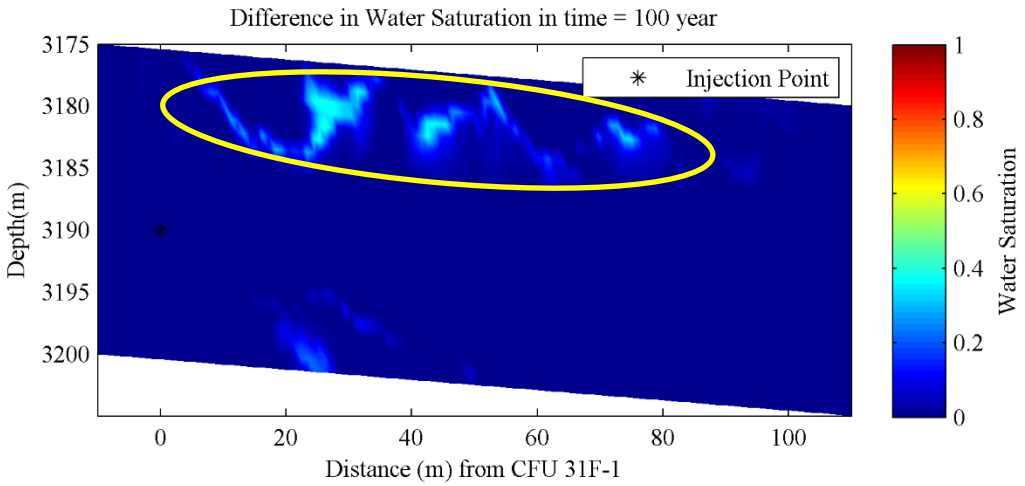

Figure 4-12: The difference between water saturation in year 100 derived with reactions and the one with no reactions. A major difference was observed at the top of the reservoir due to the reactions that affected the migration of the buoyant CO_2.

4.1.3 Forward Seismic Modeling

From the flow simulation, the time-lapse reservoir model with varying porosity and fluid saturation was obtained. Using the elastic properties and density of the each component in the reservoir as given in Table 4-2 (Mavko et al., 2009; Carter, 2014), the Reuss-Voigt-Hill average and Reuss average were used to obtain the properties of the mineral and fluid mixtures. The contents of clay were assumed to be 35% kaolinite and 65% chlorite in order to calculate the bulk modulus/shear modulus and density of clay. Clay is also reactive, but its effects is very minimal compared to that of carbonates. Lu et al. (2013) discussed that kaolinite is kinetically limited when reacting with CO_2 and discarded the kaolinite reactions when investigating geochemistry of the Cranfield minerals. We also tested using CMG-GEM to investigate on the geochemical alteration of the reservoir due to reactions solely by kaolinite. The maximum porosity change due to kaolinite was not even 1% of the change induced by the carbonates reactions. For this work,

kaolinite reactions were not considered to save computation time while running hundreds of simulations during the model selection and expansion process.

Table 4-2: The elastic moduli and densities of the minerals and fluid used in the rock physics models (Mavko et al., 2009; Carter, 2014).

Mineral/ Fluid	**Bulk Modulus (GPa)**	**Shear Modulus (GPa)**	**Density (kg/m^3)**
Quartz	36	45	2650
Clay	30.5	10.5	2800
Calcite	71	36	2710
Dolomite	76.4	49.7	2870
Brine	2.2		1045
CO_2	0.1275		675

Subsequently, the contact cement model and Hertz-Mindlin theory followed by Gassmann's theory were used to derive the elastic moduli of the saturated reservoir rock at the different time steps. Two different types of sorting trends are observed in the DAS (Carter and Spikes, 2013) as shown in Figure 4-13. Relative to well 31F-2, the region below 3195 m is a sandstone with a variation of poorly- and well-sorted formations, and above this region, is the concentric deposition of clay cement around the grains. According to this sorting trends, Carter and Spikes (2013) implemented the Hertz-Mindlin theory in the lower region and the contact cement model in the upper region. We used the same methods to characterize the elastic properties in these two regions.

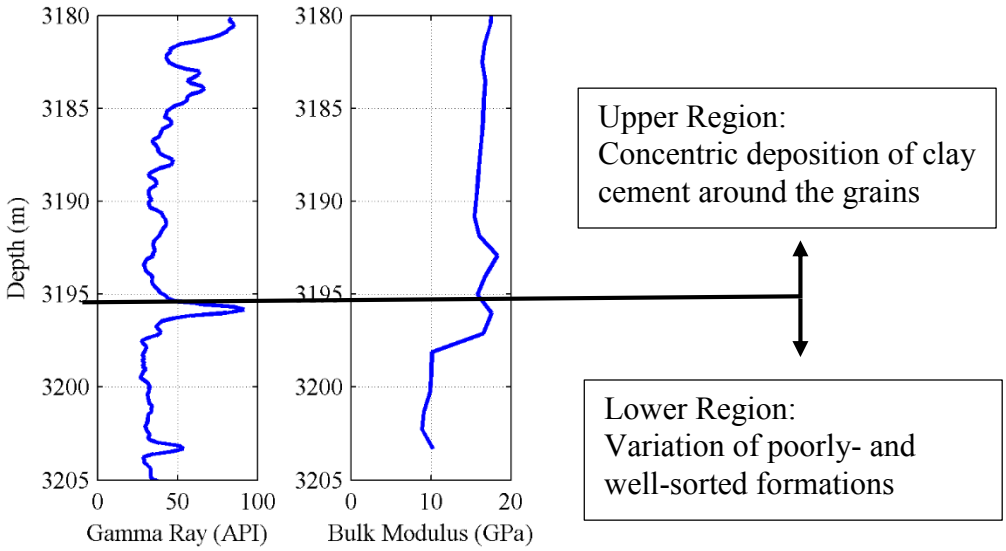

Figure 4-13: Gamma Ray log at 31F-2 and bulk modulus computed using the rock physics models according to the geology of the formation. Above 3195 m is the concentric deposition of clay cement around the grains, and the cementation theory was used. Below 3195m is the variation of poorly- and well-sorted formations, and the Hertz-Mindlin theory was used.

In order to perform forward seismic modeling, the reflection coefficient was derived in travel time coordinates from the rock properties for each layer of the reservoir. It was then convolved with a zero-phase Ricker wavelet shown in Figure 4-14. As mentioned previously, noise was neglected in the model.

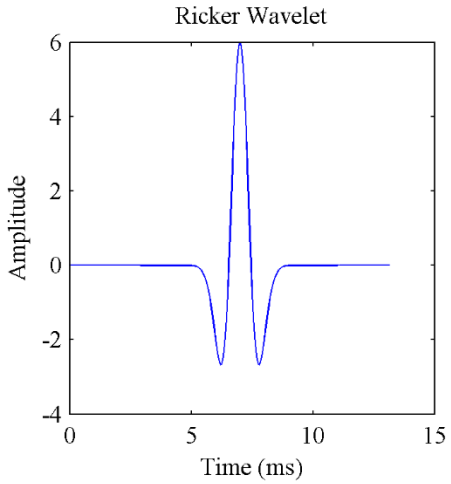

Figure 4-14: Ricker wavelet used in forward seismic modeling. The reflection coefficient derived using rock physics models was convolved with the wavelet to compute seismic response.

Figure 4-15 shows a synthetic seismogram of the DAS before injection. The two distinct regions are observed. The lower region is where there is a variation of sorting trends. The upper regions is where clay-cemented quartz grains were observed

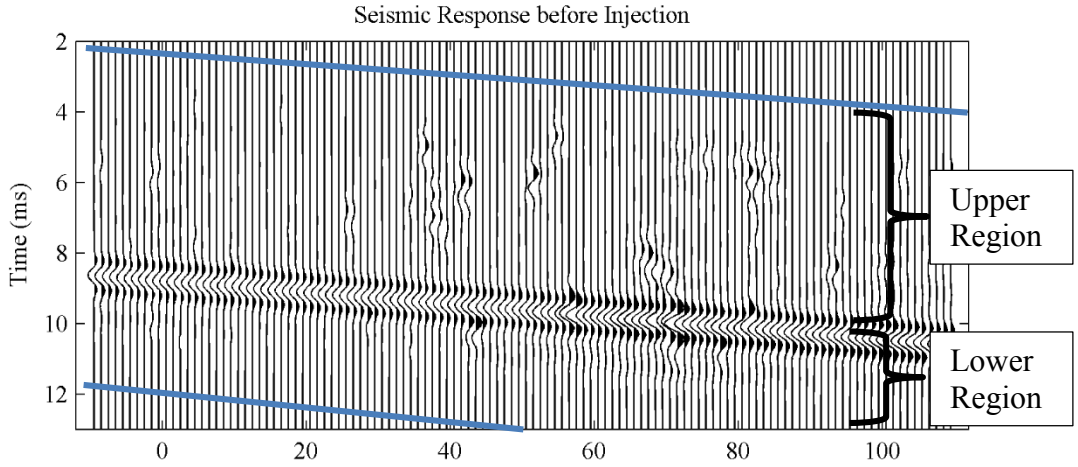

Figure 4-15: Seismic response in the DAS before injection. Blue lines indicate upper and lower boundaries of the reservoir.

Figures 4-16 and 4-17 show the synthetic seismogram of the DAS in year 50 and 100, respectively. Each figure shows (a) the seismic response of the reservoir with reactions and (b and c) comparisons between the reactive and non-reactive cases. As expected based on the observed porosity changes, the bottom ends and the top section of the reservoir showed the biggest differences between the seismic response for the reactive and non-reactive cases. These are the areas where most dissolution and precipitation occurred near the injection zone, the bottom east corner, and the top of the reservoir as indicated by orange circles. However, the major differences in seismic traces were also observed at the bottom near the center of the reservoir as indicated by blue circles. This is due to differences in water saturation between the reactive and non-reactive cases. During the reactions, there was an alteration in the rock frames and subsequently the permeability. This causes the slight differences in CO_2 migration and water saturations which affect the elastic properties and consequently, the seismic traces.

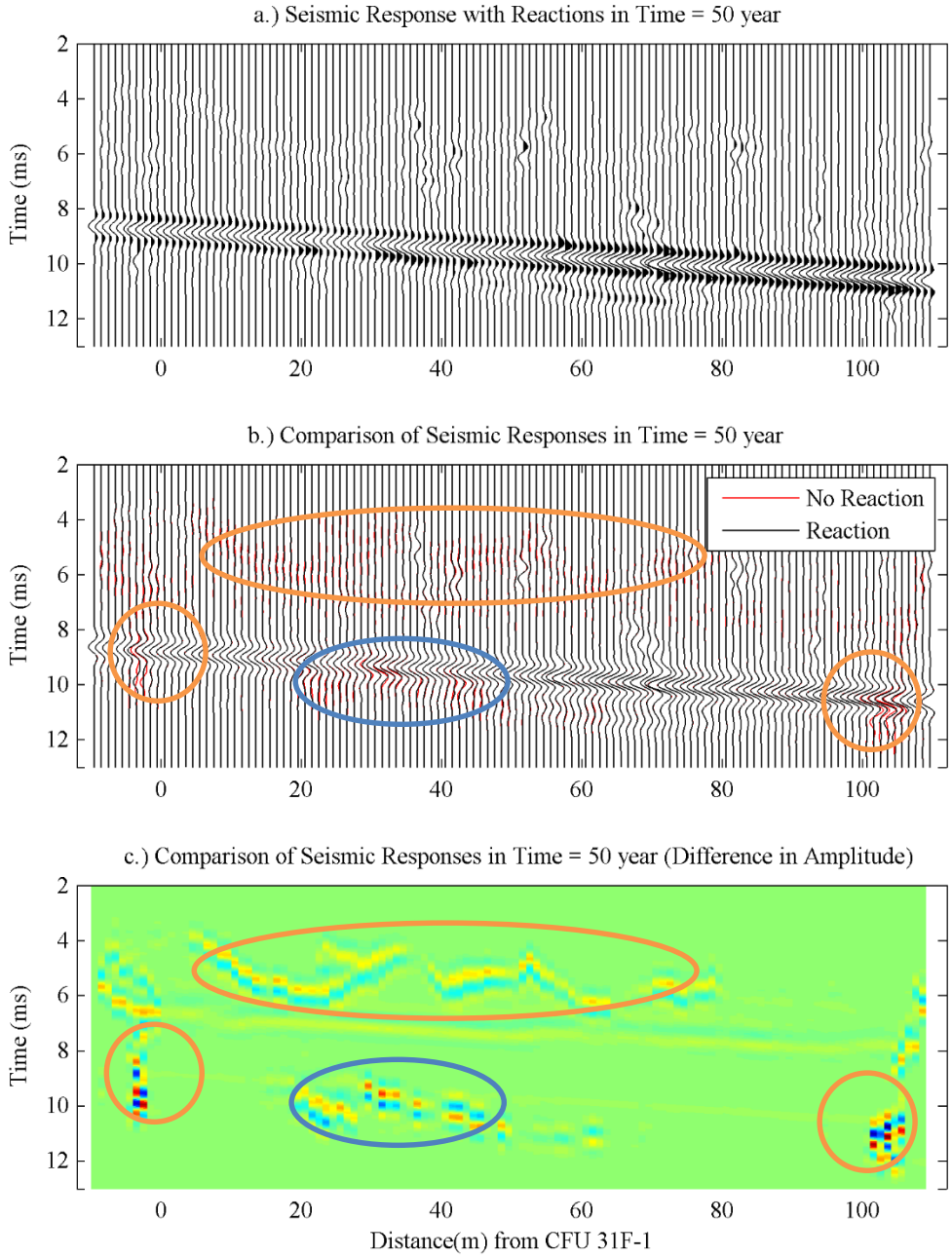

Figure 4-16: Synthetic seismogram of the reference reservoir model in year 50. Panel (a) shows the seismic response of the reservoir model with reactions present. Panel (b) and (c) show the comparison of the results for both the reactive and non- reactive cases.

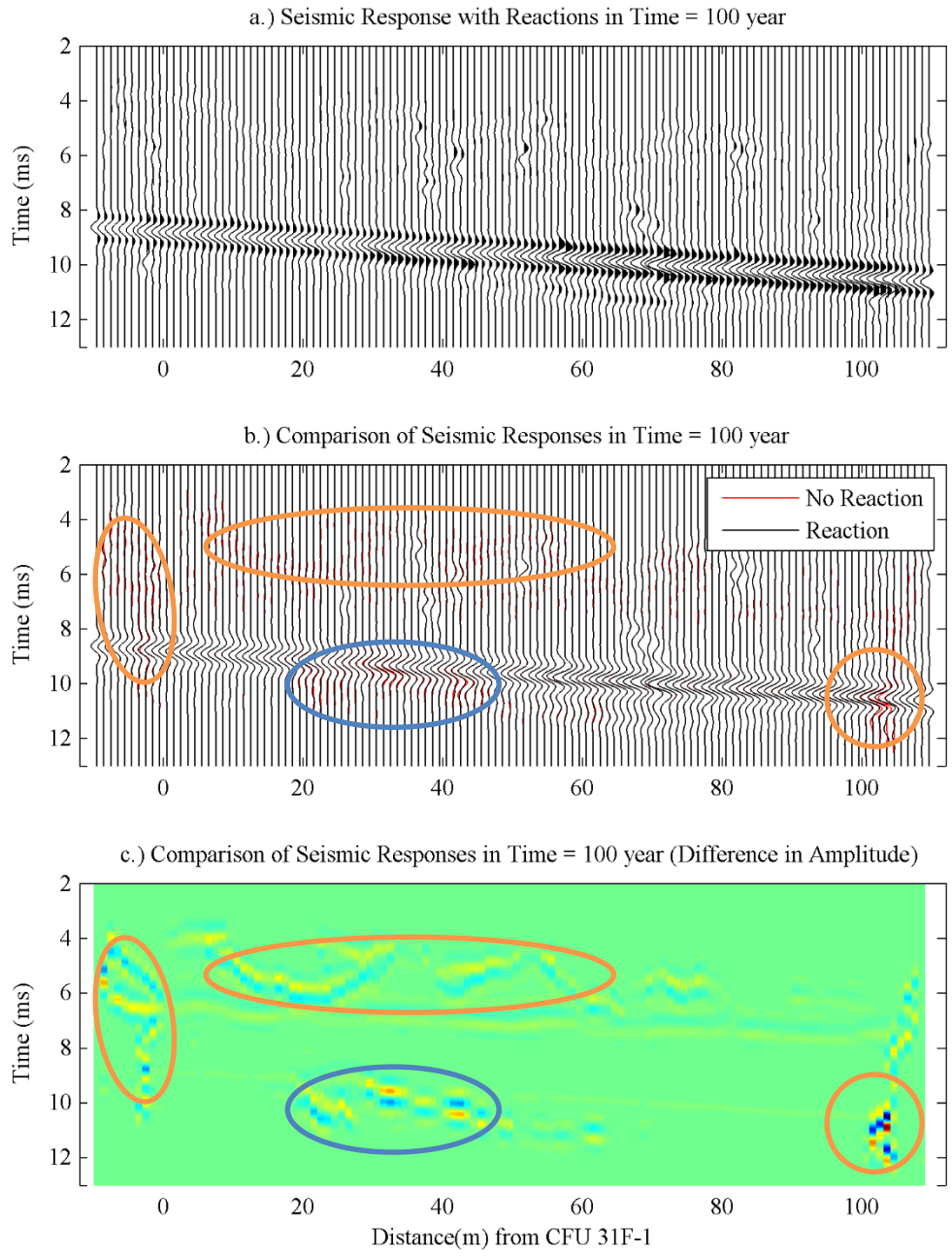

Figure 4-17: Synthetic seismogram of the reference reservoir model in year 100. Panel (a) shows the seismic response of the reservoir model with reactions present. Panel (b) and (c) show the comparison of the results for both reactive and non-reactiove cases.

4.2 Refining of the Models through Model Selection and Expansion

4.2.1 Refining the Reservoir Models before Injection

The reference model was created using sequential indicator simulation conditioned to very scarce mineralogy data. The model needs to be refined through the model selection and expansion process in order to reduce the uncertainties, especially in the carbonate facies proportions. The first step was to create a hundred prior models based on the properties of the reference model before injection. The mineralogy data of the reference model was extracted along 20 wells as shown in Figure 4-18.

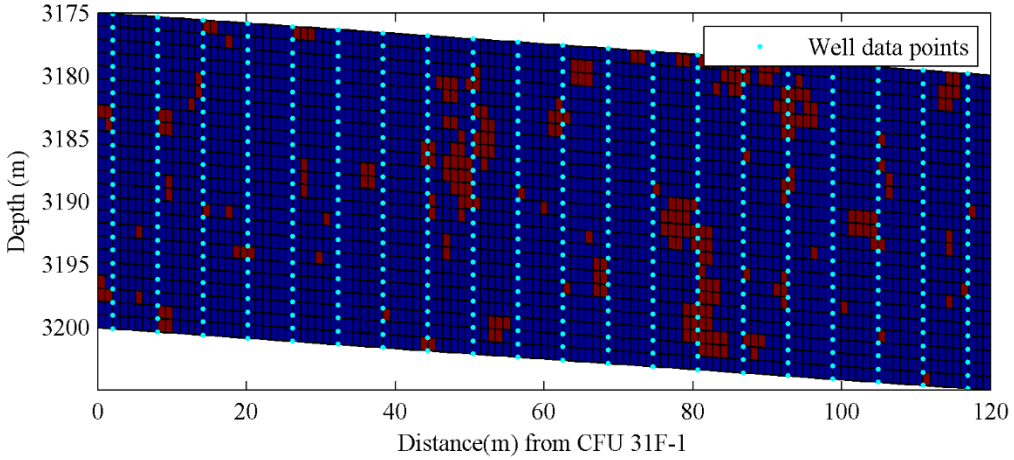

Figure 4-18: The mineralogy data of the reference model. The cyan points indicate the data points extracted to run the sequential indicator simulation to generate a subset of models.

The rock physics models and forward models were applied to all the models before injection, and the subsequent seismic responses were compared to that of the reference model. The discrete Fréchet distance was computed between the reference seismic response and that for the prior reservoir models prior to the start of injection. Figure 4-19 shows the distribution of the discrete Fréchet distance between the seismic traces of the

generated models and those of the reference model. Figure 4-20 shows the reference seismic response and the responses for the models in the first cluster from the distribution shown in Figure 4-19. The models in the first cluster was later resampled as condition data to generate a posterior set of models, which will be discussed in the proceeding section.

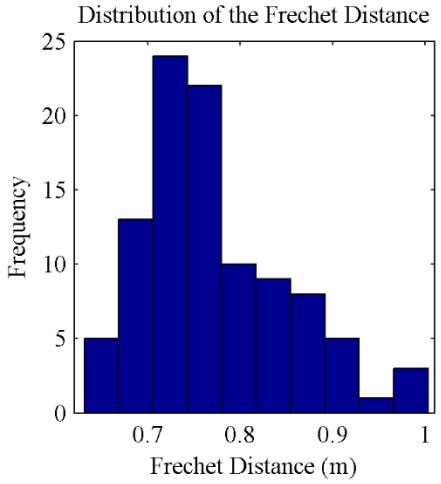

Figure 4-19: The distribution of the Fréchet distances between the reference model and the newly generated models before injection.

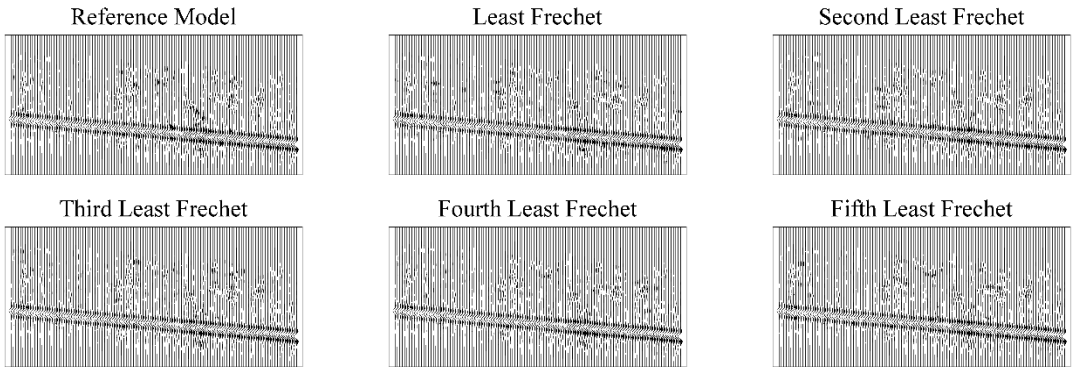

Figure 4-20: The reference seismic response (top left) and the processed seismic responses from the selected group of models. The carbonate facies data of the selected models were used to create a common variogram and to generate an expanded posterior set of reservoir models.

Out of the 100 prior models, the seismic response of the reservoir model with the least discrete Fréchet distance is shown in Figure 4-21. The discrete Fréchet distance between this model and the reference model is 0.6312. Figure 4-22 shows the facies model of the reference model and that of the model with the least discrete Fréchet distance. We were able to capture some of the regions with high carbonates proportions, but the models need to be refined to yield the better models.

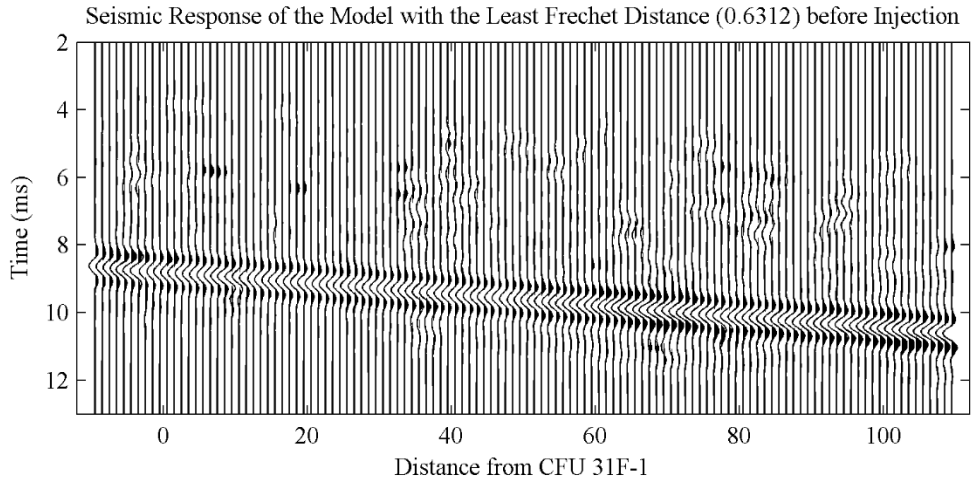

Figure 4-21: The seismic response of the model with the least discrete Fréchet distance before injection. This model is one of 100 models generated based on the data from the reference model.

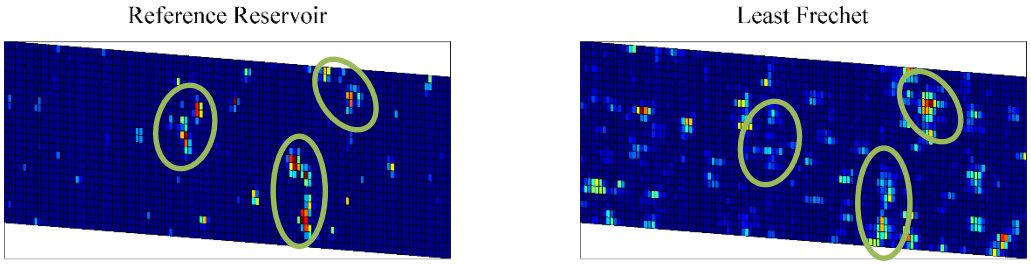

Figure 4-22: The facies model of the reference model and that of the model with the least discrete Fréchet distance. The model is able to capture some areas of high carbonates proportions, but it needs to be refined for a better performance.

4.2.2 Model Expansion

The models in the first cluster (the one with the least discrete Fréchet distance) were resampled as condition data to fit a common variogram, which was subsequently used to generate an expanded set of another 100 models. The discrete Fréchet distances between the seismic responses of the new models and that of the reference model were again compared. Figure 4-23 shows the seismic response of the model with the least discrete Fréchet distance of 0.6133 that is similar to the minimum distance that was obtained prior to model expansion. This indicates that the model expansion procedure preserves the essential characteristics of the selected group.

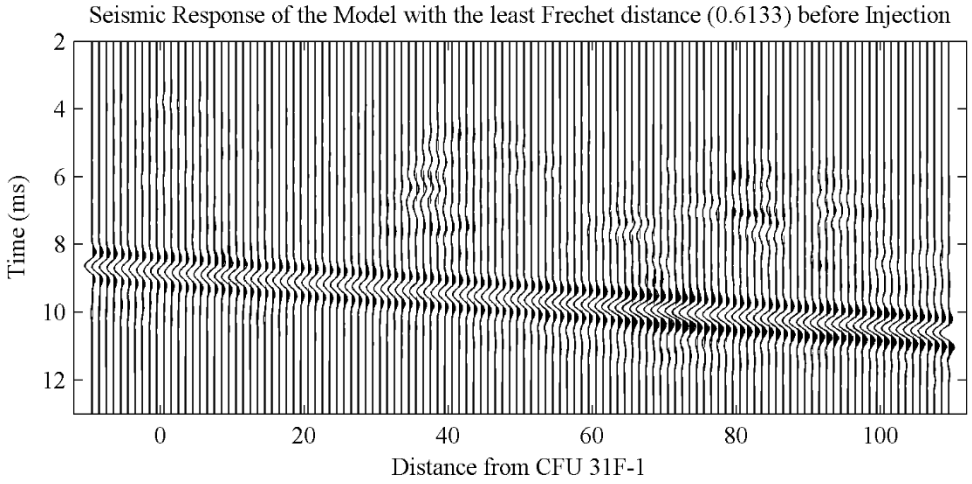

Figure 4-23: The seismic response of the refined model with the least discrete Fréchet distance before injection. This refined model is one of the expanded set of models generated using the common features of the selected cluster.

4.2.3 Refining the Reservoir Models in Year 50

Flow simulation was run on all the models in the new set of models, to observe the reservoirs' behaviors after the CO_2 injection. The seismic responses of the models in year 50 (48 years after CO_2 injection stopped) were compared with the seismic response of the reference model in year 50. The best model in the initial set and the best one in the refined

set of models are shown in Figure 4-24 and Figure 4-25. As expected, the discrete Fréchet distance was lower for the set of models selected on the basis of the seismic data at initial time. The minimum discrete Fréchet distance decreased from 0.6340 for the initial set to 0.5990 for the selected sub-set.

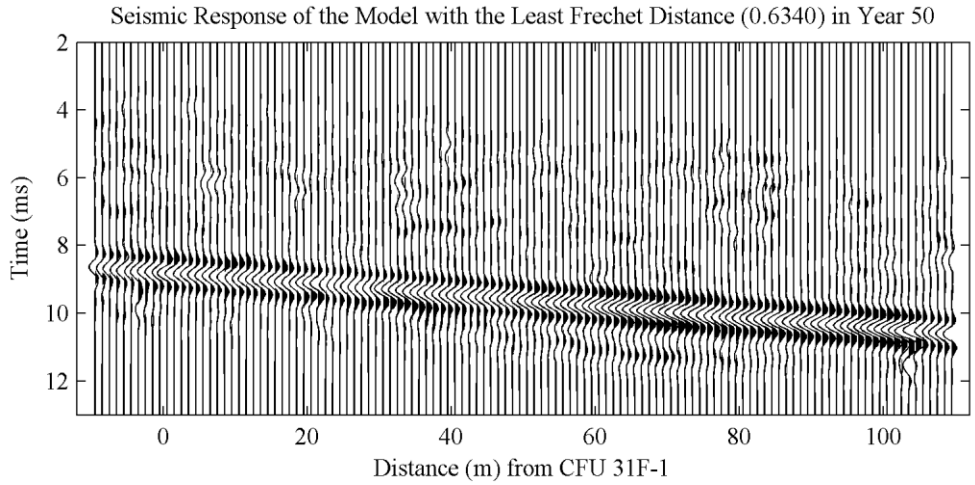

Figure 4-24: The seismic response of the model with the least discrete Fréchet distance in year 50. This model is one of 100 models in the initial set generated based on the data from the reference model.

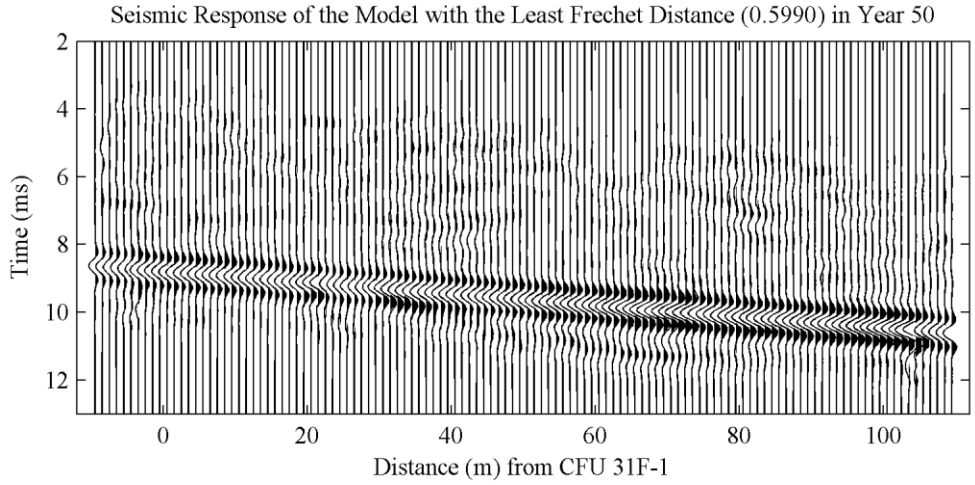

Figure 4-25: The seismic response of the selected subset of models with the least discrete Fréchet distance in year 50. The discrete Fréchet distance decreased from the previous model in Figure 4-24.

4.2.4 Refining the Reservoir Models in Years 100

The models in the new set were clustered based on the distribution of the discrete Fréchet distances in year 50. The models in the best group were again used to generate another set of 100 models. Repeating the process in the previous section, flow simulation was performed on all the models, and rock physics models and forward seismic models were used to compute the corresponding seismic responses in year 100. The seismic responses were compared with that of the reference model by computing the discrete Fréchet distances. Again, the distance was smaller for the subset of models selected using the data in year 50 as shown in Figure 4-26 and Figure 4-27, indicating that the refined models better match the reference model.

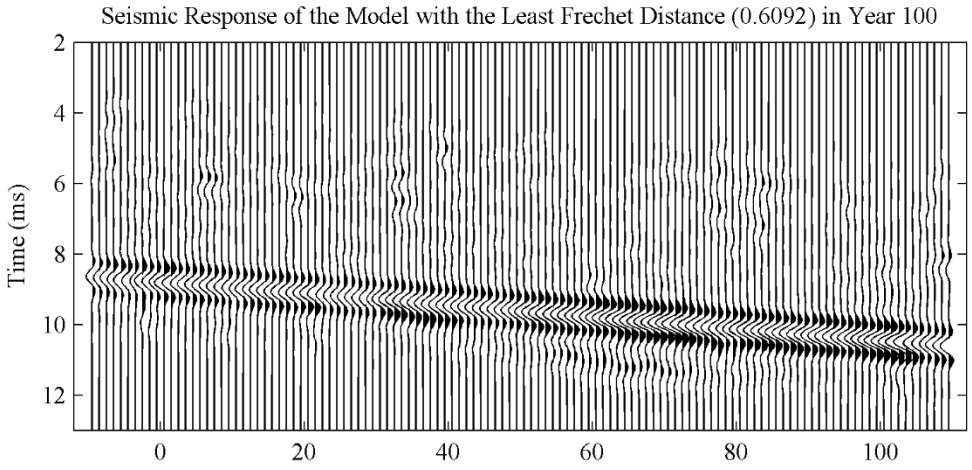

Figure 4-26: The seismic response of the model with the least discrete Fréchet distance in year 100. This model is one of 100 models in the initial set generated based on the data from the reference model.

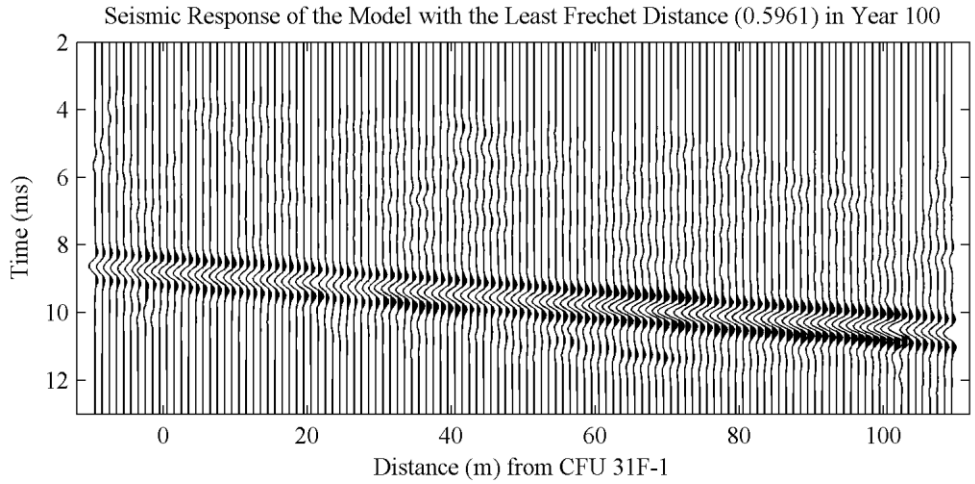

Figure 4-27: The seismic response of the with the least discrete Fréchet distance in year 100. This model belongs to the subset of models selected using the seismic response information at the end of 50 years. The discrete Fréchet distance decreased from the previous model in Figure 4-26.

Comparing the carbonate facies proportions of the reference model and those of the selected set of models, it can be observed that the refined models were able to represent the areas of high carbonate facies proportions (Figure 4-28). If the model selection and expansion is repeated until the discrete Fréchet distance between the model and the reference model is minimum, the carbonate facies proportions of the model should approximately be equal to those of the reference model. Again, it is not possible to create a reservoir model that yields seismic response that perfectly matches that of the reference model because lithology is not the only factor contributing to the changes in seismic response. The carbonates proportions, however, have the major impact on geochemistry of the reservoir, and it is essential to have information about their locations. This method allows us to predict where carbonates are present in the reservoir with the limited data available and to better assess the risks associated with storage of CO_2-saturated brine.

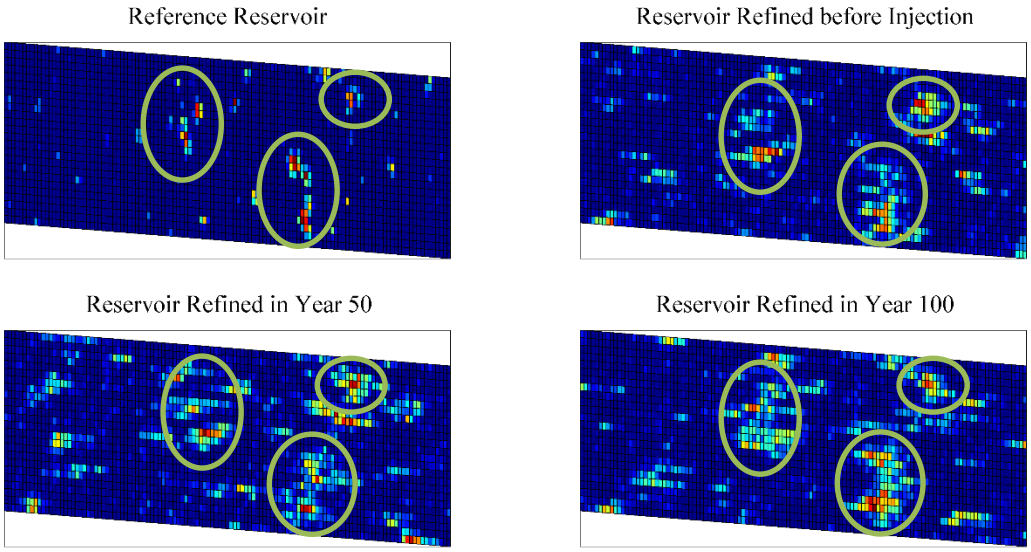

Figure 4-28: The concentration of carbonates of the reference model and the refined models. The refined models capture the areas of high proportions of carbonates. Repeating the model selection processes, the refined model that further resembles the reference model can eventually be obtained.

4.3 CONCLUSIONS

In this chapter, the impacts of CO_2 dissolved brine on the porosity and permeability of a sandstone formation with a small proportion of carbonate facies were examined. Although the carbonate facies proportion is small, the presence of these reactive facies can alter petrophysical properties of the reservoir when reacted with CO_2-saturated brine. However, there is a challenge to modelling such a reservoir because of limitation in estimating the carbonate facies proportion reliably using sparse well log data. A synthetic reservoir model was created and treated as a reference model. Time-lapse seismic modelling and workflow allowed us to compute seismic response at different times. Using the well logs of the reference model, a large suite of prior models were generated and refined through model selection and expansion processes based on their flow response and comparison to the reference model. Through this process, it was found that we were able

to reliably estimate regions where the proportion of carbonate facies is high. When this work flow is applied on the actual time-lapse data (Chapter 5), we will be able to derive an optimized reservoir model that will enable us to assess the geochemical effects of CO_2 injection and the risks associated with it.

Chapter 5: Assessing Geochemical Alterations during CO2 sequestration using Actual Time-Lapse Seismic Data and Model Selection

Calibrating reservoir models using seismic data can reduce uncertainties associated with the model and provide important geologic information (Cui and Hoffman, 2013; Lygren et al., 2002). In this chapter, the model selection procedures introduced in Chapter 4 was applied together with real inverted time-lapse seismic data available before injection and ten months after injection. Carter (2014) performed inversion in order to obtain reservoir rock properties in the form of acoustic impedance and porosity. The initial suite of reservoir models was created based on the available well information. Through the model selection and expansion process introduced in previous chapters, the initial suite of models was refined using the seismic data before injection. The best set of selected models was then used to assess the reactive transport processes associated with the migration of CO_2. The same simulation was run with no reactions, and the results were compared. The other risks associated with the CO_2 sequestration were also investigated using these models. A producer was installed in the reservoir to represent a potential leakage pathway and the breakthrough times of the CO_2 plume both for the reaction case and the non-reaction case were compared. It is demonstrated that the presence of carbonate facies even though restricted in spatial extent, plays an important role in geochemical reactions induced by CO_2 injection.

5.1 Inverted Time-Lapse Seismic Data

Carter (2014) performed inversion of the time-lapse seismic data of Cranfield to obtain the acoustic impedance and porosity. Figure 5-1 shows the acoustic impedances before injection and ten months after injection in 2010, in the region around the Designed Area of Study (DAS). The black lines indicate the approximate upper and lower boundaries

of the reservoir where CO_2 was injected. The vertical brown lines from right to left are three wells in the DAS: 31F-1, 31F-2, and 31F-3, respectively. The spacing between inlines is about 25 meters.

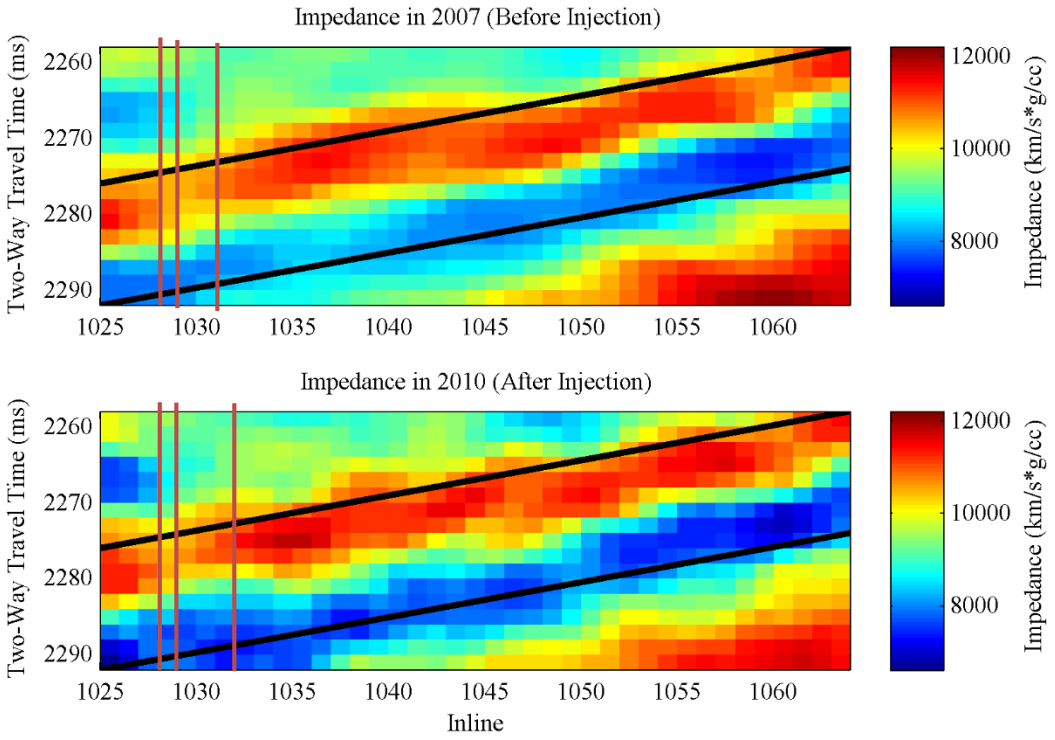

Figure 5-1: The inverted acoustic impedance before injection and ten months after injection (Carter, 2014). The black lines indicate the approximate upper and lower boundaries of the reservoir. The brown vertical lines are wells 31F-1, 31F-2, and 31F-3 from right to left, respectively.

In order to perform reactive transport simulations, it was required to transform the coordinates of the seismic data (two-way travel time and inline) into spatial metric coordinates. Given that the spacing between inlines is 25m, a new coordinate frame was defined by setting inline 1025 as 0m and inline 1065 as 1000m. It is very difficult to transform two-way travel time into depth in meters and requires velocity data inferred from Vertical Seismic Profile (VSP) log. However, given that the reservoir has 1-3^{o} dip and that

the lower boundary of the reservoir at well 31F-1 is located at the depth around 3200m, the reservoir was approximately transformed as shown in Figure 5-2. The vertical brown lines from right to left are the three wells 31F-1, 31F-2, and 31F-3, respectively.

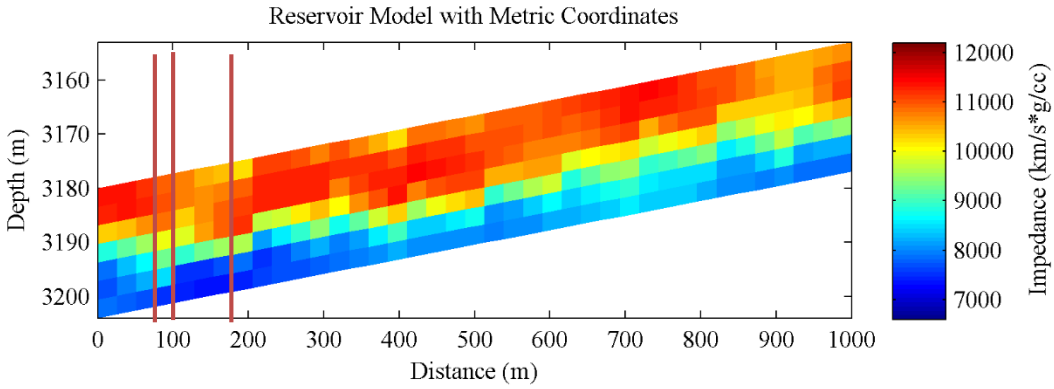

Figure 5-2: The reservoir model with the metric coordinates. The inline was transformed into horizontal distance in meters. The two-way travel time was transformed into depth in meters. The brown vertical lines are wells 31F-1, 31F-2, and 31F-3 from right to left, respectively.

In addition to acoustic impedance, spatial variation in porosity is also available by Carter (2014). However, inverted porosity is only available based on the seismic data prior to injection. The changes in porosity due to geochemical reactions were simulated using CMG-GEM and presented in the later sections of this chapter. Figure 5-3 shows the porosity variations based on seismic inversion in the DAS.

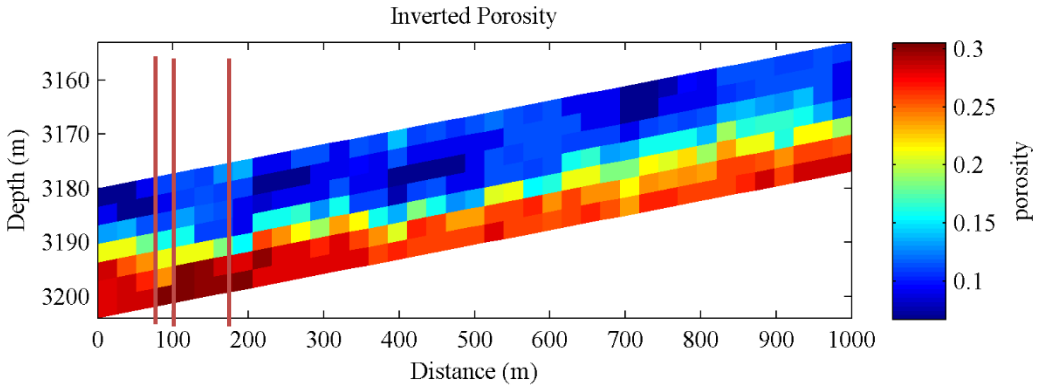

Figure 5-3: The inverted porosity in the DAS in the metric coordinates. The inline was transformed into horizontal distance in meters. The two-way travel time was transformed into depth in meters. The brown vertical lines are wells 31F-1, 31F-2, and 31F-3 from right to left, respectively.

5.2 Model Selection and Expansion

Based on the inverted acoustic impedance data before injection, ten wells were sampled as shown in Figure 5-4. The data sampled along those wells were used to create a variogram that was used to model the spatial continuity of the carbonate facies for which data was only available along well 31F-2. Figure 5-5 shows the variogram models for acoustic impedance and the carbonate facies. Table 5-1 shows the tabulated variogram model. The ranges of the impedance variogram were applied to the carbonate facies variogram. The initial variogram for the carbonate facies may not be accurate, but a better variogram was obtained through the model selection and expansion process to be discussed later.

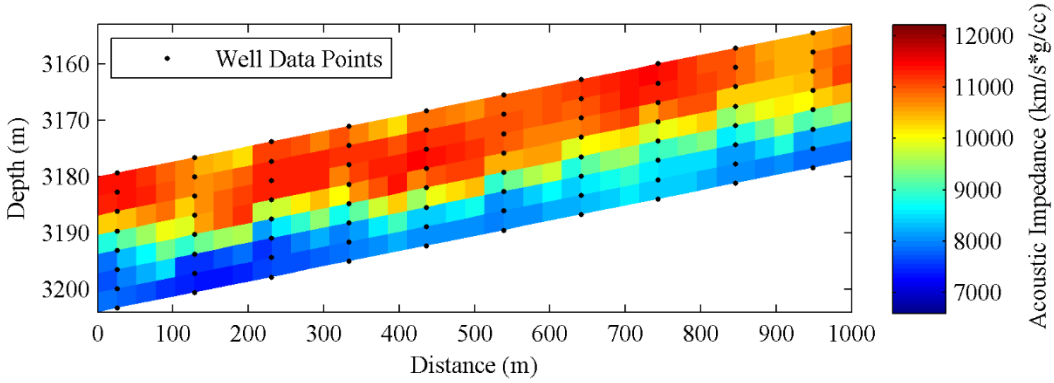

Figure 5-4: The sampling locations along which acoustic impedance values were sampled in order to create a variogram for the initial suite of models.

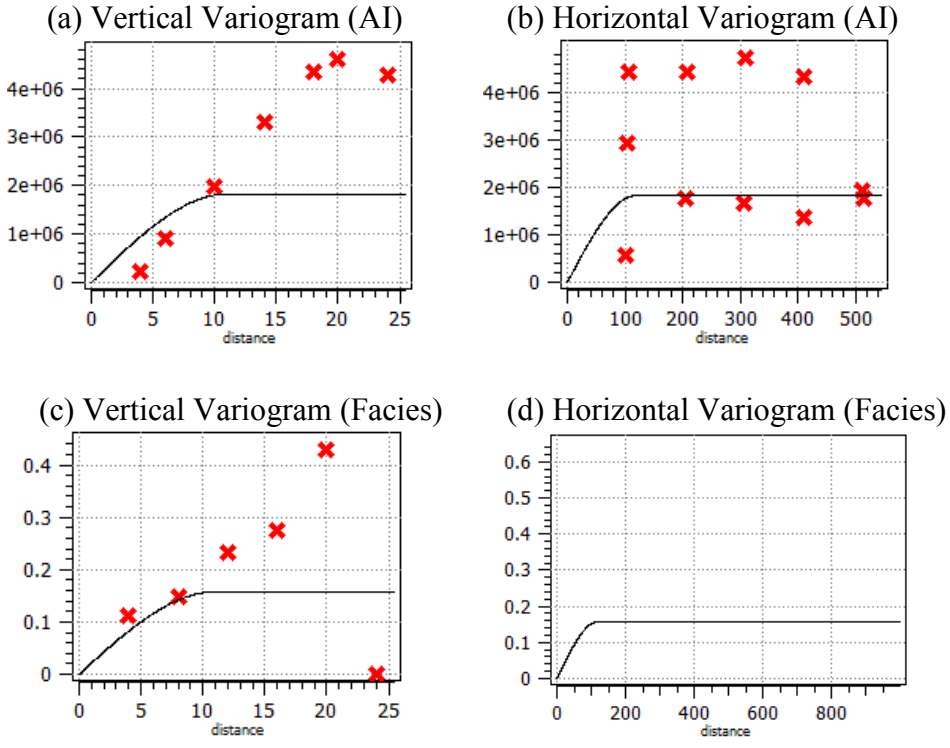

Figure 5-5: The vertical variogram model (a) and the horizontal variogram model (b) for the acoustic impedance before injection and the vertical variogram model (c) and the horizontal variogram model (d) for the carbonate facies data in 31F-2. Because the lithology data was very scarce in F31-2, the variogram of the inverted acoustic impedance was used as a guide to create the variogram for the carbonate facies.

Table 5-1: Tabulated variogram model of the acoustic impedance and carbonate facies

	Model	Nugget	Sill	a_{major}	a_{minor}	$a_{vertical}$
Acoustic Impedance	Spherical	0	1.8e6	130	50	11
Carbonate Facies	Spherical	0	0.16	130	50	11

The variogram models for the carbonate facies were applied in the sequential indicator simulation in order to generate an initial suite of reservoir models. Rock physics model was applied to all prior models in order to generate acoustic impedances and the discrete Fréchet distance was used to compare the acoustic impedances of the models with the inverted acoustic impedance before injection. Figure 5-6 shows the comparison of the first generated model and the inverted seismic data. Because of difference in sorting trends and the rock physics models used within the reservoir discussed in Chapter 4, the variability of acoustic impedance in the lower interval was different from that in the upper interval. In the upper interval, there is concentric deposition of clay cement around the grains, and in the lower interval there is a cyclicity of poorly-and well-sorted formations (Carter and Spikes, 2013). For that reason, the discrete Fréchet distance was computed separately for the upper and lower intervals, and the average was computed.

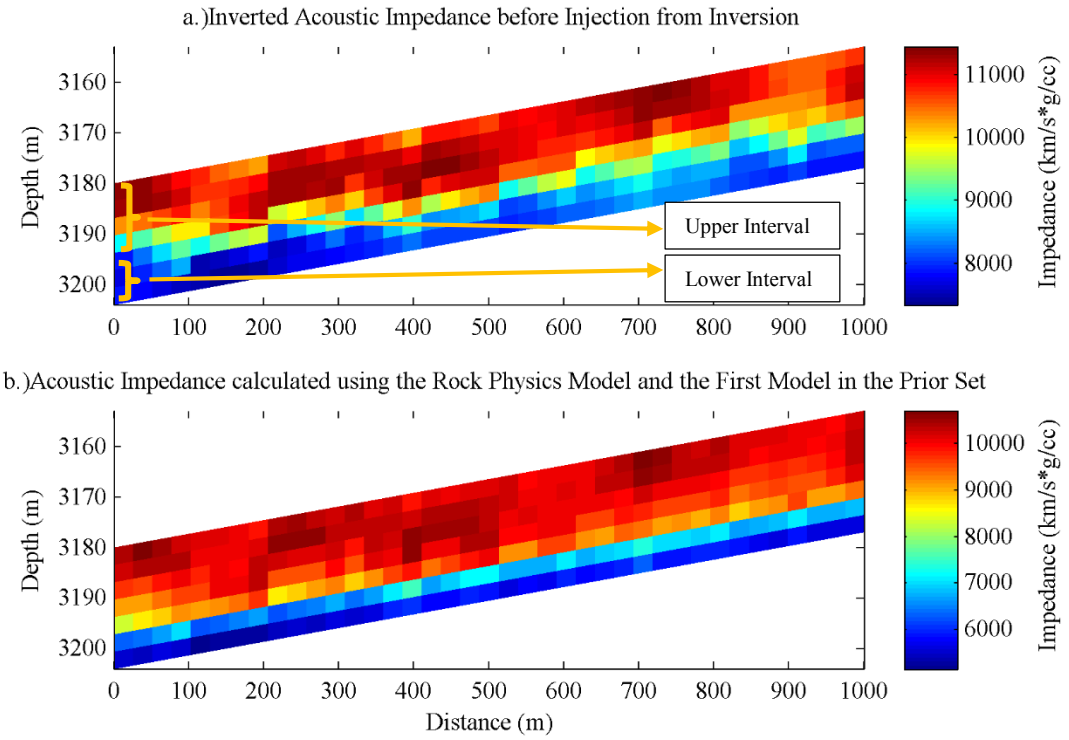

Figure 5-6: (a) The inverted acoustic impedance before injection and (b) the calculated acoustic impedance using rock physics model calculated on one of the models from the prior set. The discrete Fréchet distances were computed separately for the upper interval and the lower interval, and the average was computed. The discrete Fréchet distance between the two models in a and b was 1,051.

In order to cluster the models based on the spatial distribution of impedances, the histogram of the discrete Fréchet distance was created with 10 bins as shown in Figure 5-7. Figure 5-8 shows the inverted acoustic impedance and the processed acoustic impedance for the models falling in the first bin. The carbonate facies data from the models in the first bin were sampled as conditional data chosen to create a common variogram, which was then applied in sequential indicator simulation in order to generate an expanded posterior set of reservoir models.

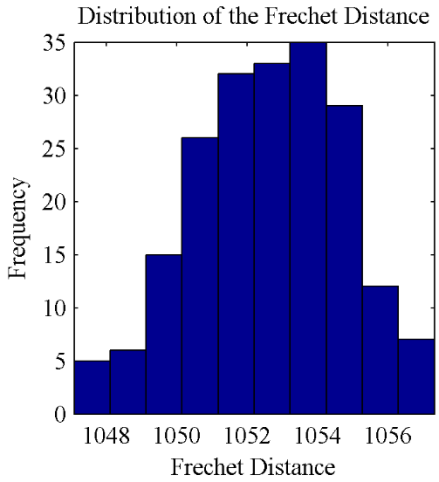

Figure 5-7: The distribution of the discrete Fréchet distances between the inverted seismic data and the rock physics calculated outputs using generated models.

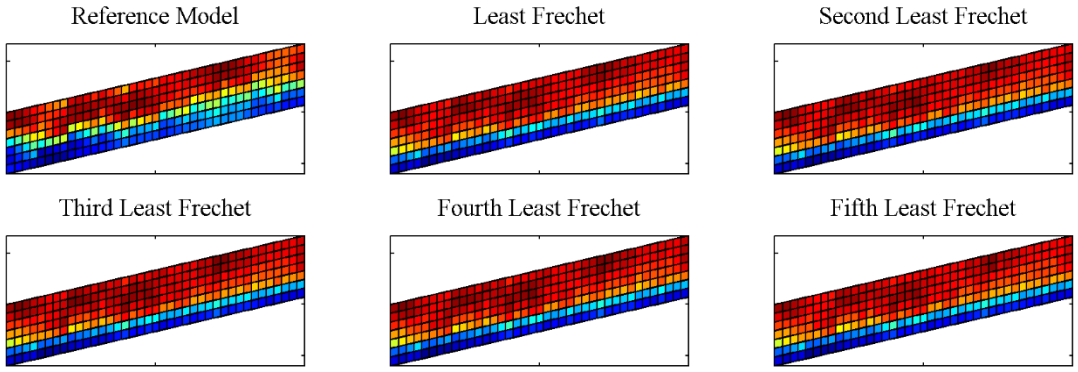

Figure 5-8: The inverted acoustic impedance (top left) and the acoustic impedances calculated using the rock physics model for the selected group of models. The carbonate facies data of the selected models were used to create a common variogram and to generate an expanded posterior set of reservoir models.

In order to verify the accuracy of the expanded set of models, the rock physics model was again applied on all the models from the posterior set, and the comparison models against the reference was again performed using the discrete Fréchet distances. The least discrete Fréchet distance between the inverted seismic response and the processed

seismic response was 1,046, which is close to the value for the original set of selected models (1,051). Figure 5-9 shows the inverted seismic response and the rock physics model-calculated values for one model from the expanded set.

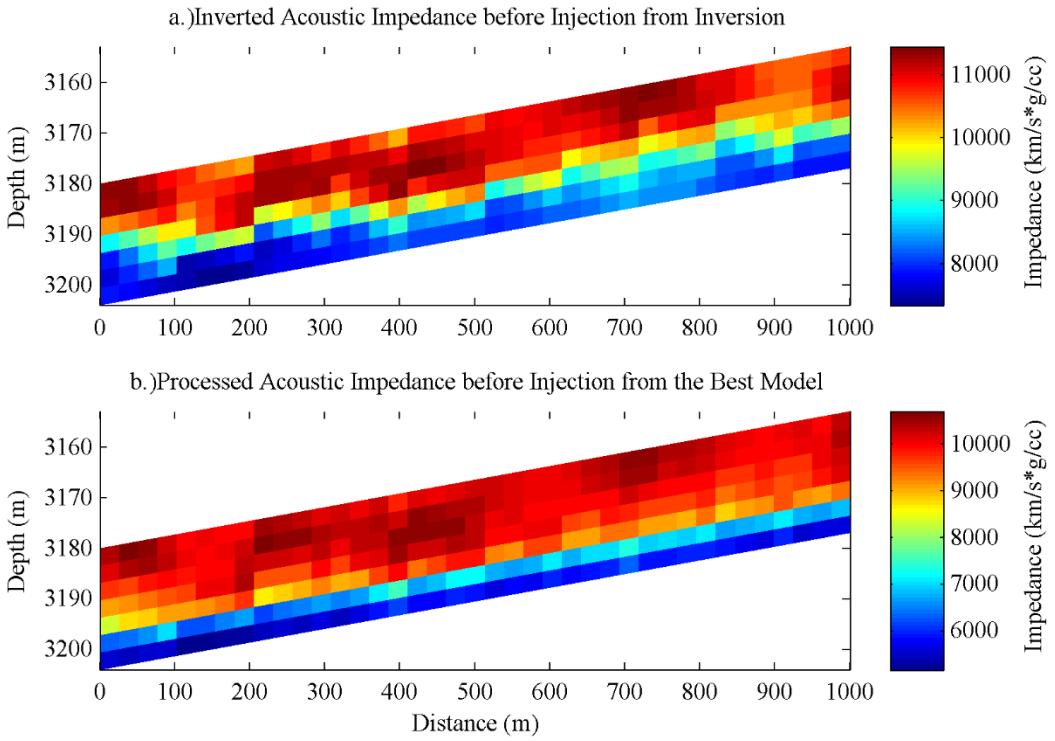

Figure 5-9: The distribution of the discrete Fréchet distances between the inverted seismic response and the processed response of the refined model.

5.2.1 Forward geochemical modeling

Using CMG-GEM, reactive transport simulations were run on all the models in the expanded set of posterior reservoir models. CO_2 was injected through well 31F-1 at one million tons-per-year rate for ten months from December 2009 to the end of September 2010, after which time a seismic survey was again completed. The changes in porosity and saturation over this period were simulated and then translated into seismic responses

through rock physics modeling. Figure 5-10 (a) shows the inverted acoustic impedance in 2010, and the processed acoustic impedances of the best-refined model in the new set of models is shown in (b). For comparison, the porosity and saturation in the first model of the prior set of models is shown in (c). The discrete Fréchet distance between the first model and the inverted acoustic impedance was 1,092. The one between the posterior set of models and the inverted acoustic impedance was 1,083, indicating that the refined models are more similar to the reference.

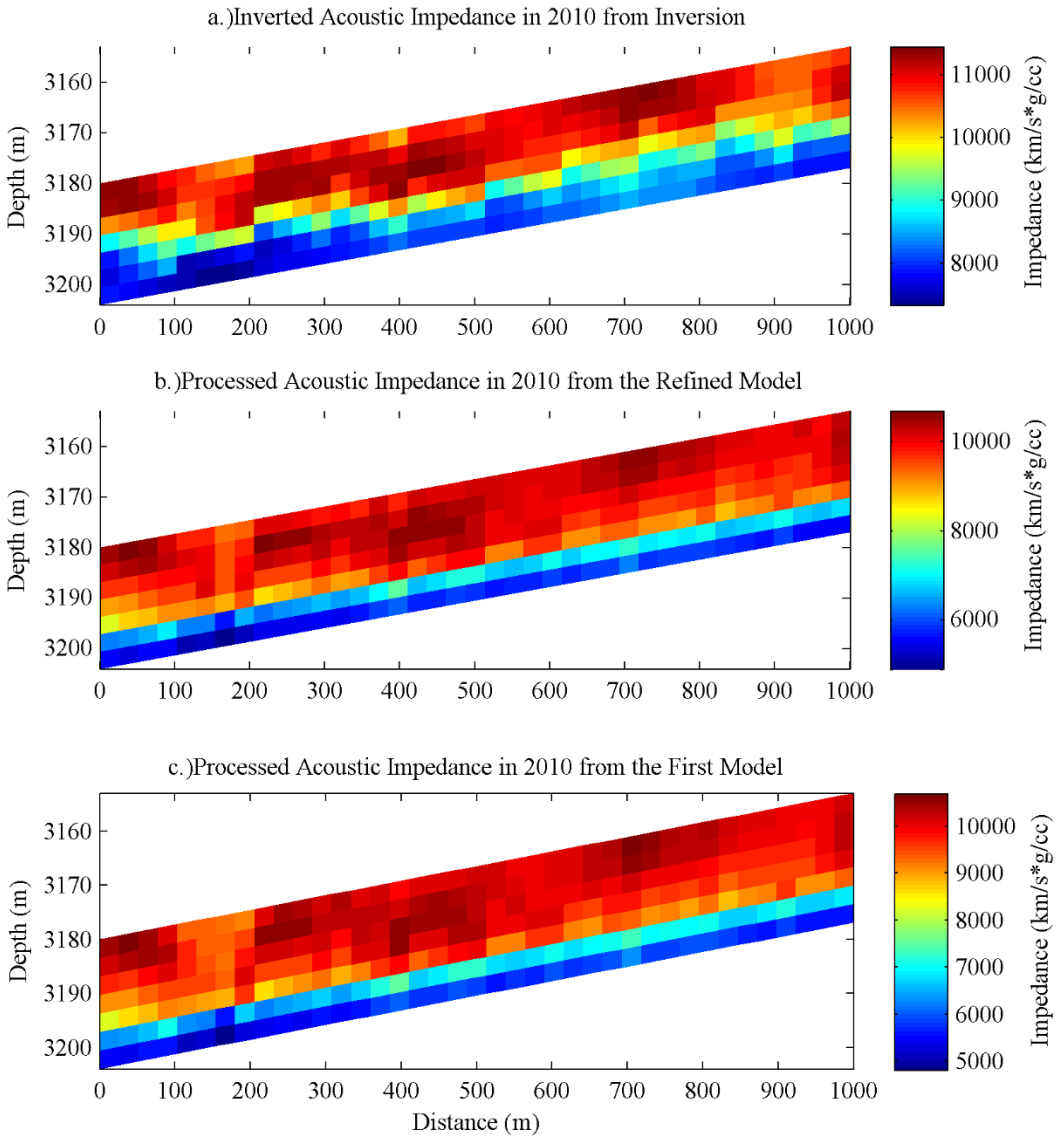

Figure 5-10: (a) The inverted acoustic impedance in 2010, (b) the acoustic impedances computed using the rock physics model for the best model in the new set of models, and (c) of the model created in the initial set. The discrete Fréchet distance decreased from 1,092 of the first model to 1,083 of the refined model.

Figure 5-11 shows the carbonate facies proportions of the refined model, which will be used for the assessment of CO_2-rock interactions and its long-term effects on sequestration.

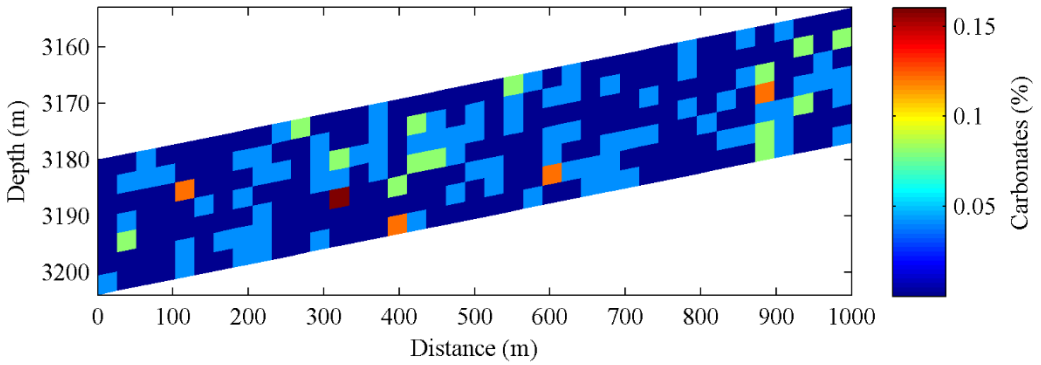

Figure 5-11: The carbonate facies proportions of the refined model. This model was used in the later sections to investigate the long-term effects of CO_2 sequestration.

5.3 Modeling and Monitoring CO_2-Rock Interactions in the Best Model

The carbonate facies model obtained in the previous section along with the inverted porosity were entered in CMG-GEM to perform reactive transport simulations in order to investigate the geochemical effects of CO_2 injection on reservoir properties. The CO_2 was injected into the bottom half of the reservoir through 31F-1 at the rate of one million tons-per-year for three years. The subsequent effects were observed for 100 years. Another simulation was run on the same model with the same injection conditions but with no reactions, and the results were compared. Acoustic impedances were calculated using the rock physics model. Figure 5-12 (a) shows the spatial distribution of acoustic impedance in 2010 with reactions while the difference between acoustic impedance derived with reactions and the one derived with no reactions is shown in Figure 5-12 (b). The difference in acoustic impedances between the two cases is partly due to the alterations in rock fabric and partly due to changes in fluid saturations. Figure 5-12 (c) shows the difference in pore structure/porosity while the difference in water saturation is shown in (d). This was ten months after injection. Most changes occurred near the injection zone as expected. The reactions induced rock frame alterations lead to porosity changes that in turn lead to changes in water saturation by affecting the fluid flow.

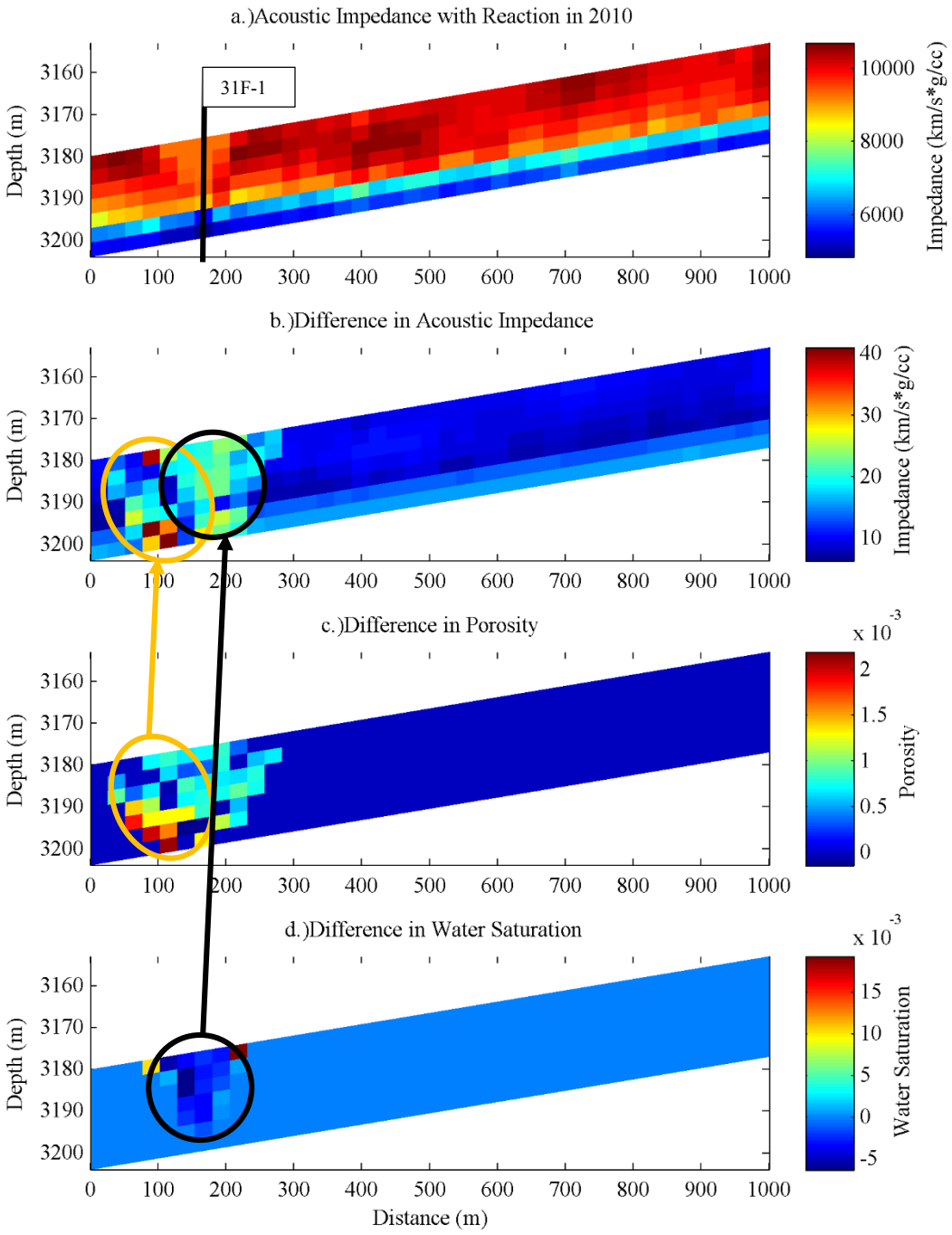

Figure 5-12: (a) Spatial distribution of acoustic impedances in 2010 corresponding to the case with reactions, (b) the difference between acoustic impedance derived with reactions and the one with no reactions, (c) the difference in porosity, and (d) the difference in water saturation.

The progressive alterations in models post-injection were also assessed. Figure 5-13 (a) shows the spatial distribution of acoustic impedances in 2059 with reactions and (b) shows the difference between acoustic impedance derived with reactions and the one derived with no reactions. The difference in porosity 50 years after injection is shown in Figure 5-13 (c) and the difference in water saturation is shown in (d). Because of relatively low density of CO_2 compared to water, the CO_2 plume migrated toward the up-dip east (right) side of the reservoir. Although rock frame alterations were observed throughout the reservoir, the major changes in porosity were observed toward the up-dip end at shallower depth. Major changes in water saturation were observed in the top portion of the reservoir. This is again due to the rock frame alterations that affect the flow of the buoyant CO_2. It induces a slight change in the rate at which the CO_2 migrates upward and this in turn introduces a change in acoustic impedance at the seismic scale.

Figure 5-14 (a) shows the spatial variation in acoustic impedance hundred years after injection (in 2109) with reactions. The difference between acoustic impedance derived in models with reactions and in models with no reactions is depicted in Figure 5-14 (b). The difference in porosity is shown in Figure 5-14 (c) while the difference in water saturation is shown in (d). Slight differences in the reservoir are observed between the models in 2059 and the one in 2109 indicating that there are ongoing reactions in the reservoir long after the injection. The results thus show the importance of modeling reactive transport when predicting reservoir fluid migration. In the short term and long term, the effects were clearly visible at the seismic scale.

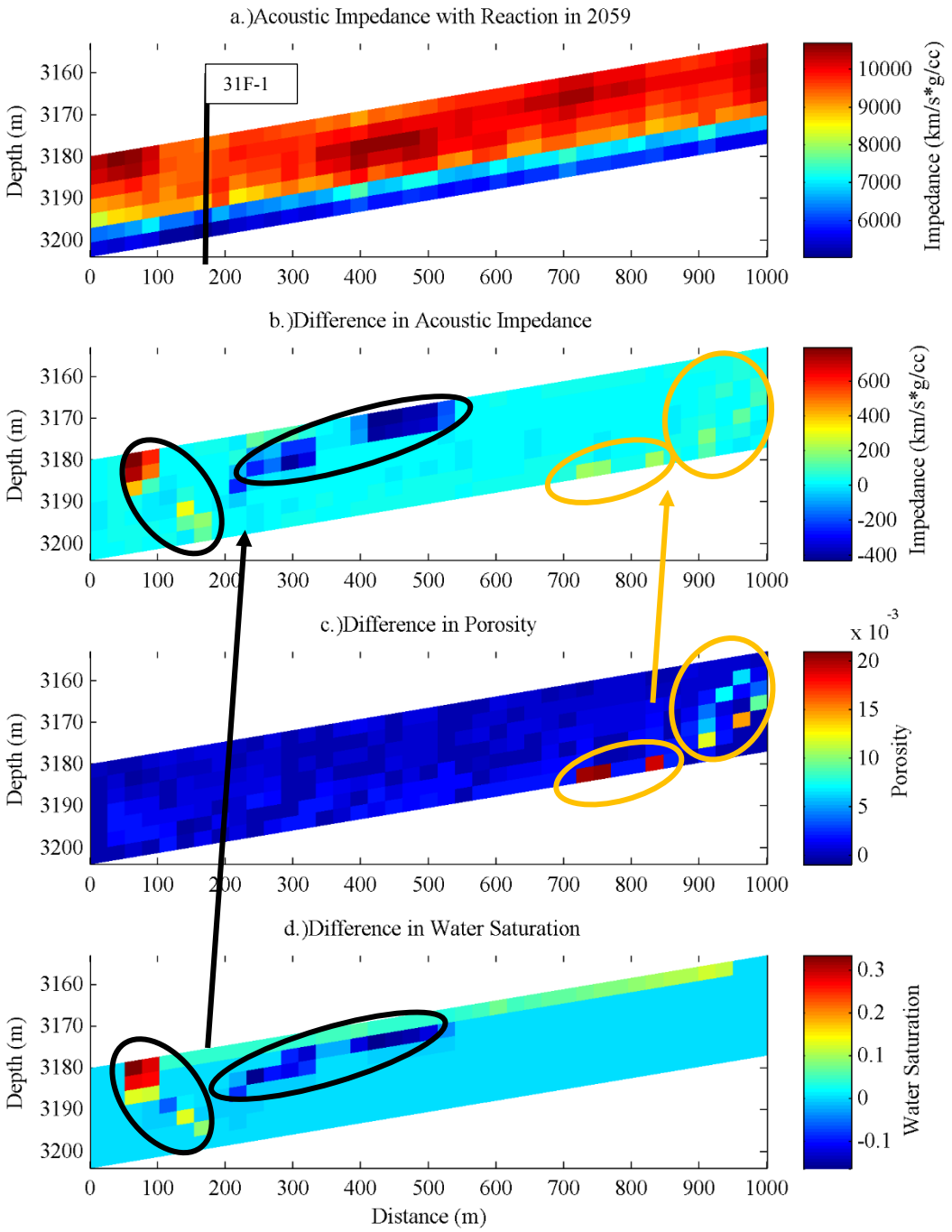

Figure 5-13: (a) Acoustic impedance in 2059 (50 years after injection) with reactions, (b) the difference between acoustic impedance derived with reactions and the one derived with no reactions, (c) the difference in porosity, and (d) the difference in water saturation.

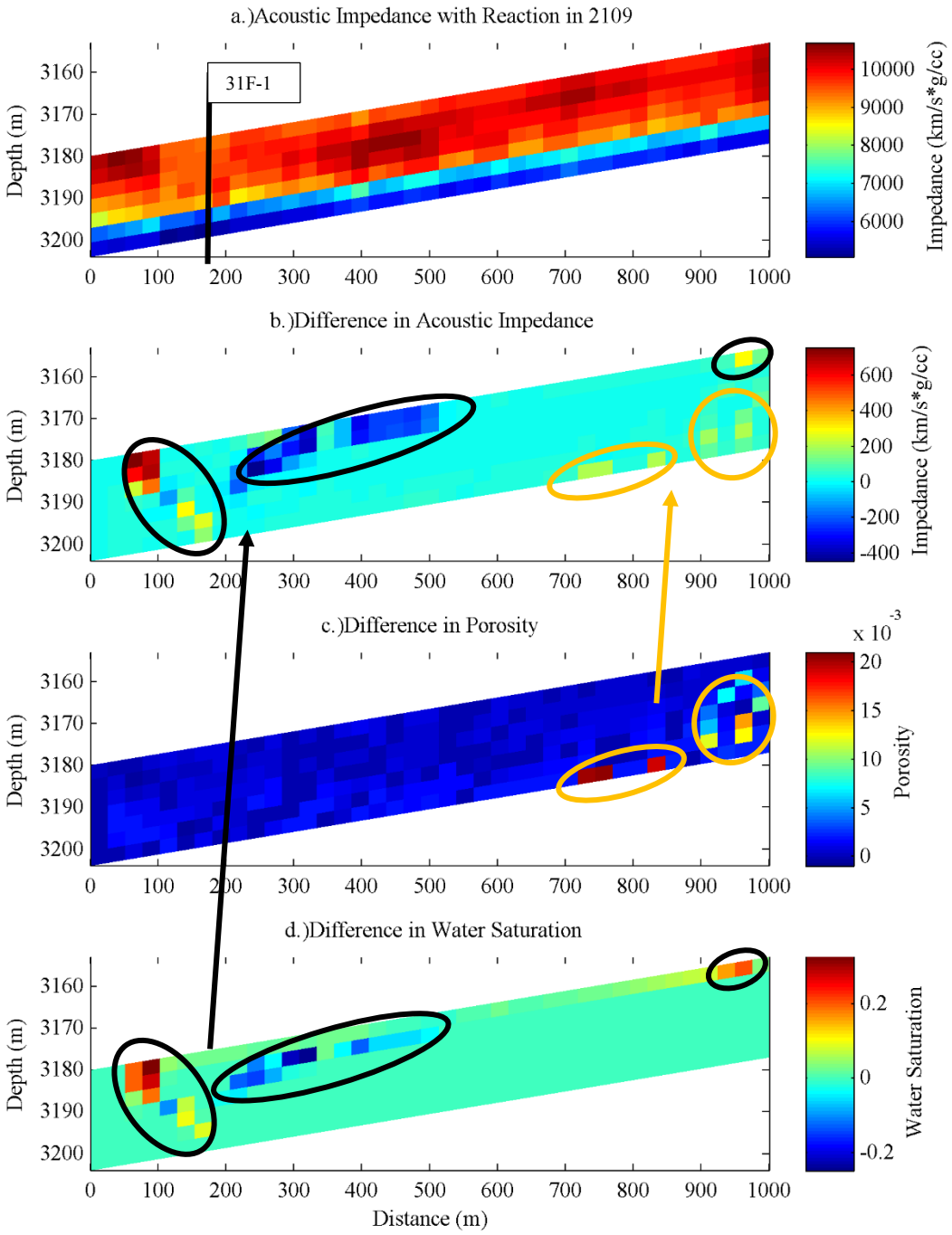

Figure 5-14: (a) Acoustic impedance in 2109 (100 years after injection) with reactions, (b) the difference between acoustic impedance derived with reactions and the one derived with no reactions, (c) the difference in porosity, and, (d) the difference in water saturation.

5.4 Assessment of Leakage Pathways

In order to assess the impact of geochemical reactions on leakage flux from the reservoir, the same simulation was performed with a producer placed in the reservoir as shown in Figure 5-15. The producer represents a possible fault or leakage pathway that might be present in the reservoir but very difficult to detect. The leakage flux (i.e. CO_2 escaping) through such a pathway was investigated for both the reaction and no reaction cases.

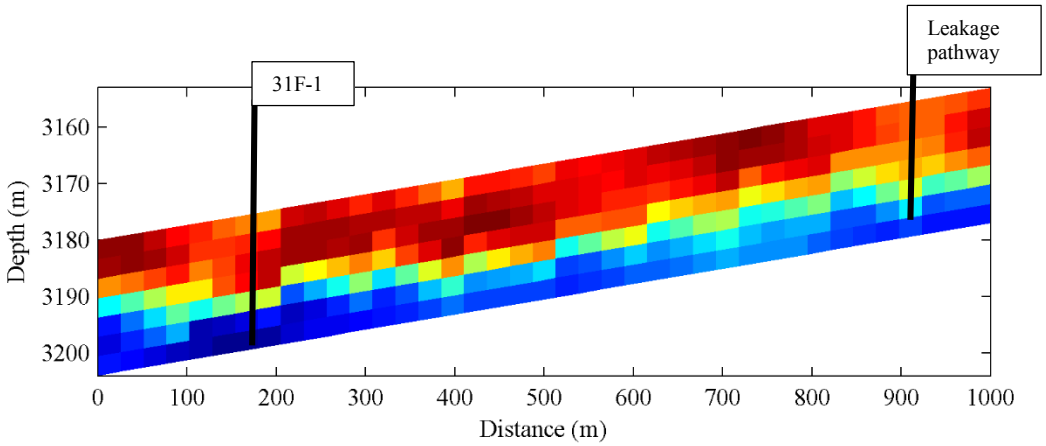

Figure 5-15: The reservoir with a leakage pathway. The breakthrough time of CO_2 and the amount of gas escaped into the pathway was compared for the reaction case and for the no reaction case.

Figure 5-16 shows the cumulative amount of gas that escaped through the leakage pathway some time after injection began. From the figure, it is observed that $0.5m^3$ CO_2 escaped after 1,308 days after injection for the no reaction case and 1,313 days after injection for reaction case, showing a 5 day difference. This again shows that the flow of CO_2 was affected by the reactions that induced rock frame alterations.

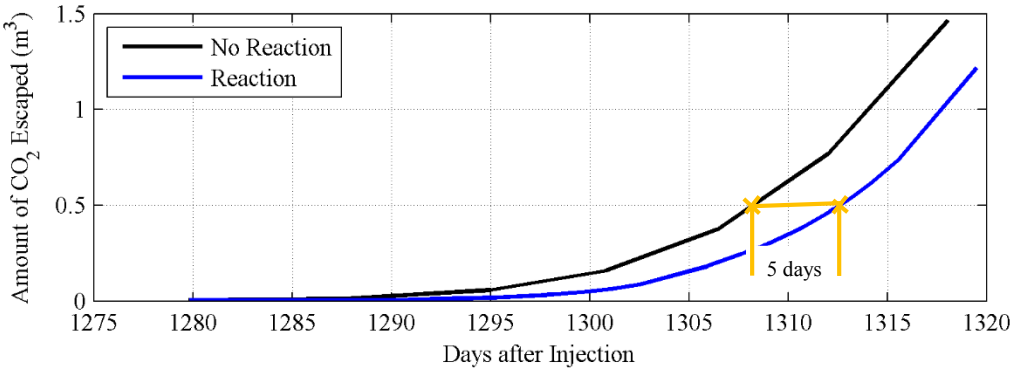

Figure 5-16: The cumulative CO_2 escaped from the reservoir for two models: one considering reactions and the other not considering reactions.

5.5 CONCLUSIONS

In this chapter, time-lapse acoustic impedances inverted from the real seismic data for the Cranfield site were used to pin-point locations of geochemical alterations. The model selection and expansion process introduced in Chapter 3 and shown in Chapter 4 through the synthetic case were applied on the real data set from Cranfield. The time-lapse seismic modelling and workflow allowed us to pick a subset of models that exhibit similar rock physics properties as observed in the seismically inverted acoustic impedance data. The selected carbonate facies models were then used to assess the impact of reactive transport of the reservoir due to the flow of CO_2-saturated brine in the long term. It was shown through this study that the impact of reactions due to even small proportions of carbonate facies in the reservoir was visible at the seismic scale, e.g. in acoustic impedance. The impact of geochemical reactions on leakage flux through an arbitrary leakage pathway was also evaluated. A producer was placed in a reservoir model, and the CO_2 flux was observed. The results indicate that frame alterations due to reactions causes a re-distribution of subsurface fluids and a consequent delay in the time taken for the leakage flux to reach a threshold value.

Chapter 6: Conclusion and Recommendations for Future Work

6.1 CONCLUSIONS

When modeling CO_2 sequestration in siliciclastic reservoirs with very small proportions of carbonate facies, the impact of reactive transport is often ignored. The impact of mineral reactions on the risk of leakage or conversely, the mitigation of risk of CO2 leakage because of blockage of leakage pathways by reaction products, compels the study of such reservoir rock alterations. The minerals can be dissolved and/or precipitated to alter the rock frames (e.g. changes in porosity and permeability) and therefore affect the flow of the fluid in the reservoir. When predicting location of leakage pathways and estimating the amount of CO_2 leaking out of the formation, ignoring reactions in modeling can yield erroneous result.

In this research, we investigated the geochemical effects of CO2/brine mixtures in subsurface formations and based our study on data obtained for the siliciclastic reservoir in Cranfield, Mississippi. The reservoir has a very small proportion of carbonate facies. We investigated the behavior of the reservoir using a commercial compositional simulator CMG-GEM. We studied both reactive and non-reactive cases and the effect of rock frame alteration on the rock physics properties of the formation. With the limited data available for the Cranfield reservoir, we implemented a unique model selection and expansion scheme to progressively refine our estimates of likely carbonate facies locations within the reservoir. With the well log data, an initial suite of models was generated. The models were then processed through a flow model and rock physics model in order to transform the mechanical and flow properties of the rock into the corresponding seismic response, i.e. acoustic impedance, The models were clustered based on their similarity with the actual seismic impedance data available for the field, and the models in the closest cluster were used to generate an expanded posterior set of models. Through the model selection and

expansion scheme, we were able to obtain a carbonate facies model that was similar to the reference model.

Subsequently, a model was selected from the expanded set of posterior models and was used to assess the geochemical alterations of the siliciclastic reservoir due to long-term sequestration of CO_2. The dissolution and precipitation of the carbonate facies altered the rock frames of the reservoir and affected the flow of CO_2- saturated brine. To further assess the impact of reactions, a leakage pathway was placed in the reservoir, and the simulations were run corresponding to both reaction and no reaction cases. The difference in the breakthrough time of CO_2 and the amount of gas escaping through the pathway was significantly different for the reactive and non-reactive cases. The flux was reduced and the breakthrough time was increased in the reactive flow case because of re-distribution of the CO_2-brine mixture due to alterations in rock frame. It was clearly seen through this work that the effects of the presence of carbonate facies, even in small proportions, could be manifested in the reservoir response at the seismic scale and should be carefully modeled when investigating CO_2 sequestartion.

6.2 Recommendations for Future Work

- The simulation of reactive transport of the reservoir was performed using CMG-GEM in this work. Other simulators that are capable of compositional modeling, such as PHREEQC and COMSOL could also be used. Using different simulators and comparing the results would give useful information about the accuracy of the flow simulations.
- There were uncertainties in modeling geochemical reactions in the reservoir. Parameters such as reactive surface area, equilibrium constants, and activation energy, etc. were estimated using the previous simulations performed on a

reservoir similar to that of Cranfield due to limitations in inferring these parameters using the field samples. To correctly model geochemical reactions specifically to Cranfield reservoirs, the field samples should be used in laboratory scale experiments in order to obtain more accurate geochemical parameters.

- The main focus of this research work was on the Designed Area of Study (DAS) in Cranfield which is a small area within the entire Cranfield. There are over 40 wells drilled elsewhere within the field for oil and gas recovery. It is recommended that the model selection aspect of the research be performed using information from these other wells also in order to improve the robustness of the posterior set of models.

Nomenclature

Parameters

a	Range of continuity
Cov	Covariance
F	Conditional probability
f	Fraction of material
$\underline{h}$	Lag distance
I	Indicator variable
K	Bulk Modulus (GPa)
M	Elastic Modulus (GPa)
n	Number of contacts per grain
R_0	Reflection coefficient
S	Saturation
S_n, S_τ	Grain composite stiffness parameters
T	Seismic trace
t	Time (sec)
$\underline{u}$	Variable location
V	Velocity (km/s)
w	Wavelet
Z	Random function variable

Greek Symbols

α	Cement deposition parameter
δ_{dF}	Discrete Fréchet distance
γ	Variogram
σ	Error variance
ϕ	Porosity
ϕ_0	Critical porosity
λ	Weights to minimize error variance
μ	Shear modulus (GPa)
ν	Poisson's ratio
ρ	Density (g/cm^3)

Subscripts

0	Mineral
c	Cement
dry	Dry rock
fl	Fluid
g	Grain
HM	Hertz-Mindlin
P	P-wave
S	S-wave
sat	Saturated rock
w	Water

References

Ajo-Franklin, J. B., J. Peterson, J. Doetsch, and T. M. Daley. 2013. "High-Resolution Characterization of a CO2 Plume Using Crosswell Seismic Tomography: Cranfield, MS, USA." *International Journal of Greenhouse Gas Control* 18. Elsevier Ltd: 497–509. doi:10.1016/j.ijggc.2012.12.018.

Alt, Helmut, and Michael Godau. 1992. "Measuring the Resemblance of Polygonal Curves." *8th Annual Computational Geometry* 6/92: 102–9.

Berg, Robert, and Billy Cook. 1962. "Petrography and Origin of Lower Tuscaloosa Sandstones, Mallalieu Field, Lincoln County, Mississippi." *Gulf Coast Association of Geological Societies Transactions* 18: 242–44.

Berryman, J G. 1995. "Mixture Theory for Rock Properties." *AGU Handbook of Physical Constants*, 205–28.

Berryman, James G. 1999. "Origin of Gassmann S Equations." *Geophysics* 64 (5): 1627–29. http://citeseerx.ist.psu.edu/viewdoc/download?doi=10.1.1.80.5400&rep=rep1&type=pdf.

Boucher, S. 1974. "On the Effective Moduli of Isotropic Two-Phase Elastic Composites." *Journal of Composite Materials* 8 (1): 82–89. doi:10.1177/002199837400800108.

Buchin, Kevin, Maike Buchin, Rolf Van Leusden, Wouter Meulemans, and Wolfgang Mulzer. 2013. "Computing the Fréchet Distance with a Retractable Leash," 1–13.

Carrigan, Charles R., Xianjin Yang, Douglas J. LaBrecque, Dennis Larsen, David Freeman, Abelardo L. Ramirez, William Daily, et al. 2013. "Electrical Resistance Tomographic Monitoring of CO2 Movement in Deep Geologic Reservoirs." *International Journal of Greenhouse Gas Control* 18. Elsevier Ltd: 401–8. doi:10.1016/j.ijggc.2013.04.016.

Carter, Russell W., and Kyle T. Spikes. 2013. "Sensitivity Analysis of Tuscaloosa Sandstones to CO2 Saturation, Cranfield Field, Cranfield, MS." *International Journal of Greenhouse Gas Control* 18 (October). Elsevier Ltd: 485–96. doi:10.1016/j.ijggc.2013.01.006.

Carter, Russell Wirkus. 2014. "Fluid Characterization at the Cranfield CO 2 Injection Site : Quantitative Seismic Interpretation from Rock-Physics Modeling and Seismic Inversion." The University of Texas at Austin.

"Causes of Climate Change." 2014. *The United States Environmental Protection Agency*. Accessed December 1. http://www.epa.gov/climatechange/science/causes.html.

Chilès, Jean-Paul, and Pierre Delfiner. 2012. *Geostatistics: Modeling Spatial Uncertainty*. Second Edi. Hoboken, NJ, USA: John Wiley & Sons, Inc.

Computer, Modeling Group Ltd. 2013. *Compositional & Unconventional Reservoir Simulation*. Calgary.

Cui, Q, B Todd Hoffman, and T L Davis. 2013. "Quantitative Time-Lapse Seismic Integrated History Match in Delhi Field." *SPE Western Regional & AAPG Pacific Section Meeting 2013 Joint Technical Conference*, no. April: 1–14.

De Silva, G.P.D., P.G. Ranjith, and M.S.a. Perera. 2015. "Geochemical Aspects of CO2 Sequestration in Deep Saline Aquifers: A Review." *Fuel* 155. Elsevier Ltd: 128–43. doi:10.1016/j.fuel.2015.03.045.

Delshad, Mojdeh, Xianhui Kong, Reza Tavakoli, Seyyed a. Hosseini, and Mary F. Wheeler. 2013. "Modeling and Simulation of Carbon Sequestration at Cranfield Incorporating New Physical Models." *International Journal of Greenhouse Gas Control* 18. Elsevier Ltd: 463–73. doi:10.1016/j.ijggc.2013.03.019.

Doetsch, Joseph, Michael B. Kowalsky, Christine Doughty, Stefan Finsterle, Jonathan B. Ajo-Franklin, Charles R. Carrigan, Xianjin Yang, Susan D. Hovorka, and Thomas M. Daley. 2013. "Constraining CO2 Simulations by Coupled Modeling and Inversion of Electrical Resistance and Gas Composition Data." *International Journal of Greenhouse Gas Control* 18. Elsevier Ltd: 510–22. doi:10.1016/j.ijggc.2013.04.011.

Dvorkin, Jack, and Amos Nur. 1996. "Elasticity of High-Porosity Sandstones: Theory for Two North Sea Data Sets." *Geophysics* 61 (5): 1363. doi:10.1190/1.1444059.

Egermann, P., B. Bazin, and O. Vizika. 2005. "An Experimental Investigation of Reaction-Transport Phenomena During CO2 Injection." *14th SPE Middle East Oil and Gas Show and Conference, 12-15 March*. doi:10.2118/93674-MS.

Eiter, Thomas, and Heikki Mannila. 1994. "Computing Discrete Fréchet Distance."

Fréchet, M.R. 1906. "Sur Quelques Points Du Calcul Fonctionnel." *Rendiconti Del Circolo Mathematico Di Palermo* 22: 1–74.

Gassmann, Fritz. 1951. "Über Die Elastizität Poröser Medien." *Vierteljahrsschrift Der Naturforschenden Gesellschaft* 96 (1): 1–23. http://www.ngzh.ch/archiv/1951_96/96_1/96_2.pdf.

Gharbi, Oussama, Branko Bijeljic, Edo Boek, and Martin J. Blunt. 2013. “Changes in Pore Structure and Connectivity Induced by CO2 Injection in Carbonates: A Combined Pore-Scale Approach.” *Energy Procedia* 37 (0). Elsevier B.V.: 5367–78. doi:10.1016/j.egypro.2013.06.455.

Grombacher, Denys, Tiziana Vanorio, and Yael Ebert. 2012. “Time-Lapse Acoustic, Transport, and NMR Measurements to Characterize Microstructural Changes of Carbonate Rocks during Injection of CO[sub 2]-Rich Water.” *Geophysics* 77 (3): WA169. doi:10.1190/geo2011-0281.1.

Gunter, W.D., Stefan Bachu, D.H.-S. Law, Vinod Marwaha, D.L. Drysdale, D.E. Macdonald, and T.J. McCann. 1996. “Technical and Economic Feasibility of CO2 Disposal in Aquifers within the Alberta Sedimentary Basin, Canada.” *Energy Conversion and Management* 37 (6-8): 1135–42. doi:10.1016/0196-8904(95)00311-8.

Hashin, Z., and S. Shtrikman. 1963. “A Variational Approach to the Theory of the Elastic Behaviour of Multiphase Materials.” *Journal of the Mechanics and Physics of Solids* 11 (2): 127–40. doi:10.1016/0022-5096(63)90060-7.

Holtz, Mark H, Vanessa Núñez López, and Caroline L Breton. 2005. “Moving Permian Basin Technology to the Gulf Coast : The Geologic Distribution of CO 2 EOR Potential in Gulf Coast Reservoirs.”

Hosseini, Seyyed Abolfazl, Hamidreza Lashgari, Jong W. Choi, Jean Philippe Nicot, Jiemin Lu, and Susan D. Hovorka. 2013. “Static and Dynamic Reservoir Modeling for Geological CO2 Sequestration at Cranfield, Mississippi, U.S.A.” *International Journal of Greenhouse Gas Control* 18. Elsevier Ltd: 449–62. doi:10.1016/j.ijggc.2012.11.009.

Hosseini, Seyyed Abolfazl, Simon a. Mathias, and Farzam Javadpour. 2012. “Analytical Model for CO2 Injection into Brine Aquifers-Containing Residual CH4.” *Transport in Porous Media* 94 (3): 795–815. doi:10.1007/s11242-012-0025-x.

Hovorka, Susan D. 2013. “Three-Million-Metric-Ton-Monitored Injection at the Secarb Cranfield Project—Project Update.” *Energy Procedia* 37 (0). Elsevier B.V.: 6412–23. doi:http://dx.doi.org/10.1016/j.egypro.2013.06.571.

Isaaks, Edward H., and R. Mohan Srivasatava. 1989. *An Introduction to Applied Geostatistics*. New York: Oxford University Press.

Kordi, M. 2013. “Characterization and Prediction of Reservoir Quality in Chlorite-Coated Sandstones : Evidence from the Late Cretaceous Lower Tuscaloosa Formation at Cranfield Field , Mississippi , U . S . A .” The University of Texas at Austin.

Kuster, Guy T., and M. Nafi Toksöz. 1974. “Velocity and Attenuation of Seismic Waves in Two Phase Media: Part II. Experimental Results.” *GEOPHYSICS* 39 (5): 607–18. doi:10.1190/1.1440451.

Lu, J., M. Kordi, S.D. Hovorka, T.A. Meckel, and C.A. Christopher. 2013. “Reservoir Characterization and Complications for Trapping Mechanisms at Cranfield CO2 Injection Site.” *International Journal of Greenhouse Gas Control* 18 (October): 361–74. doi:10.1016/j.ijggc.2012.10.007.

Lu, Jiemin, Yousif K. Kharaka, James J. Thordsen, Juske Horita, Athanasios Karamalidis, Craig Griffith, J. Alexandra Hakala, et al. 2012. “CO 2-Rock-Brine Interactions in Lower Tuscaloosa Formation at Cranfield CO 2 Sequestration Site, Mississippi, U.S.A.” *Chemical Geology* 291: 269–77. doi:10.1016/j.chemgeo.2011.10.020.

Lu, Jiemin, Kitty Milliken, Robert M. Reed, and Susan Hovorka. 2011. “Diagenesis and Sealing Capacity of the Middle Tuscaloosa Mudstone at the Cranfield Carbon Dioxide Injection Site, Mississippi, U.S.A.” *Environmental Geosciences* 18 (1): 35–53. doi:10.1306/eg.09091010015.

Lygren, M, E Lindeberg, P Bergmo, G V Dahl, K Å Halvorsen, T Randen, and L Sønneland. 2002. “History Matching of CO 2 Flow Models Using Seismic Modeling and Time-Lapse Data History Matching of CO 2 Flow Models Using Seismic Modeling and Time-Lapse Data.” In *SEG Annual Meeting*. Denver.

Mandalaparty, Prashanth, Milind Deo, and Joseph Moore. 2011. “Gas-Compositional Effects on Mineralogical Reactions in Carbon Dioxide Sequestration.” *SPE Journal* 16 (4). doi:10.2118/124909-PA.

Mavko, Gary, Tapan Mukerji, and Jack Dvorkin. 2009. *The Rock Physics Handbook: Tools for Seismic Analysis of Porous Media*. 2nd ed. New Tork: Cambridge University Press.

Mindlin, R. D. 1949. “Compliance of Elastic Bodies in Contact.” *Trans. ASME*, no. 71. New York, NY: Springer New York: A – 259. doi:10.1007/978-1-4613-8865-4_24.

Mito, Saeko, Ziqiu Xue, and Takashi Ohsumi. 2008. “Case Study of Geochemical Reactions at the Nagaoka CO2 Injection Site, Japan.” *International Journal of Greenhouse Gas Control* 2 (3): 309–18. doi:10.1016/j.ijggc.2008.04.007.

Nghiem, Long, Peter Sammon, Jim Grabenstetter, and Hiroshi Ohkuma. 2004. "Modeling CO2 Storage in Aquifers with a Fully-Coupled Geochemical EOS Compositional Simulator." *Proceedings of SPE/DOE Symposium on Improved Oil Recovery*. doi:10.2118/89474-MS.

Parkhurst, D.L., and C.A.J. Appelo. 2013. "Description of Input and Examples for PHREEQC Version 3—A Computer Program for Speciation, Batch-Reaction, One-Dimensional Transport, and Inverse Geochemical Calculations." In *U.S. Geological Survey Techniques and Methods*. http://pubs.usgs.gov/tm/06/a43/.

Reuss, A. 1929. "Berechnung Der Fließgrenze von Mischkristallen Auf Grund Der Plastizitätsbedingung Für Einkristalle ." *ZAMM - Zeitschrift Für Angewandte Mathematik Und Mechanik* 9 (1): 49–58. doi:10.1002/zamm.19290090104.

Roscoe, R. 1952. "The Viscosity of Suspensions of Rigid Spheres." *British Journal of Applied Physics* 3 (8): 267–69. doi:10.1088/0508-3443/3/8/306.

Ryan, Harold. 1994. "Ricker, Ormsby; Klander, Butterworth -A Choice of Wavelets." *Recorder* September: 24–25. doi:209.91.124.56.

Singh, Harpreet, and Sanjay Srinivasan. 2014. "SPE-169133-MS Scale up of Reactive Processes in Heterogeneous Media - Numerical Experiments and Semi-Analytical Modeling Description of Case Study."

Spooner Jr., Harry. 1964. "Basal Tuscaloosa Sediments, East-Central Louisiana." *AAPG Bulletin* 48: 1963. doi:10.1306/BC743BBF-16BE-11D7-8645000102C1865D.

Vanorio, Tiziana, Amos Nur, and Yael Ebert. 2011. "Rock Physics Analysis and Time-Lapse Rock Imaging of Geochemical Effects due to the Injection of CO[sub 2] into Reservoir Rocks." *Geophysics* 76 (5): O23. doi:10.1190/geo2010-0390.1.

Vialle, Stphanie, and Tiziana Vanorio. 2011. "Laboratory Measurements of Elastic Properties of Carbonate Rocks during Injection of Reactive CO2-Saturated Water." *Geophysical Research Letters* 38 (1): 1–5. doi:10.1029/2010GL045606.

Voigt, W. 1906. "Bestimmung Der Elastizitätskonstanten von Eisenglanz." *Annalen Der Physik* 327 (1): 129–40. doi:10.1002/andp.19063270108.

Wang, Tianye, Huaiyuan Wang, Fengjun Zhang, and Tianfu Xu. 2013. "Simulation of CO2-Water-Rock Interactions on Geologic CO2 Sequestration under Geological Conditions of China." *Marine Pollution Bulletin* 76 (1-2). Elsevier Ltd: 307–14. doi:10.1016/j.marpolbul.2013.08.014.

Wolff, Eric, Inez Fung, Brian Hoskins, John Mitchell, Tim Palmer, and Benjamin Santer. 2014. “Climate Change: Evidence & Causes.” *The Royal Society and the US National Academy of Sciences*. http://dels.nas.edu/resources/static-assets/exec-office-other/climate-change-full.pdf.

Zhang, Rui, Ranjana Ghosh, Mrinal K. Sen, and Sanjay Srinivasan. 2013. “Time-Lapse Surface Seismic Inversion with Thin Bed Resolution for Monitoring CO2 Sequestration: A Case Study from Cranfield, Mississippi.” *International Journal of Greenhouse Gas Control* 18 (July 2008). Elsevier Ltd: 430–38. doi:10.1016/j.ijggc.2012.08.015.